Universidade do Minho
Escola de Ciências

Nelssom Fernandez da Cunha

Vibrational modes of compounds materials C-H

Vibrational modes of compounds materials C-H
Nelssom Fernandez da Cunha
UMinho|2018

dezembro de 2018

Universidade do Minho
Escola de Ciências

Nelssom Fernandez da Cunha

Vibrational modes of compounds materials C-H

Dissertação de Mestrado
Mestrado em Física
Ramo em Física Aplicada

Trabalho realizado sob orientação do
Professor Doutor Mikhail I. Vasilevskiy
e da
Professora Doutora Maria de Fátima G. Cerqueira

dezembro de 2018

Declaration

Nome: Nelssom Fernandez da Cunha

Endereço electrónico: pg31421@alunos.uminho.pt
Telefone: (H) (+351) 253 637 285 · (M) (+351) 927 496 106
Número do Cartão de cidadão: 14 163 763

Título dissertação: Vibrational modes of compounds materials C-H

Orientador: Professor Doutor Mikhail I. Vasilevskiy
Orientadora: Professora Doutora Maria de Fátima G.Cerqueira

Ano de conclusão: 2018

Designação do Mestrado: Mestrado em Física - Ramo de Física Aplicada

Braga, Dezembro de 2018

Nelssom Fernandez da Cunha

Acknowledgments

Firstly, I would like to thank my advises the possibility of work in this project, Professor Dr. Mikhail I. Vasilevskiy, and Professor Maria de Fátima G. Cerqueira, for the opportunity to do this work and for all support given, guidance and advice, during the development of the work. My thanks for their help and involvement in this project, allowing to develop excellent results in the end.

My thanks to Dr. Manuel Melle Franco, University of Aveiro, for helpful discussions and providing DFT data on interbond angles and electric charges for hydrogen in basal chemisorption state.

My thanks to Prof. Luis Vieira for FTIR measurements.

My thanks to Dr. Eduardo Alves, ITN, University of Lisbon, for arranging ERDA measurements.

I would also like to thank the support and encouragement of my friends, my parents, and my sister.

And finally, I would like to thank the availability and attention of the Physics Department office every morning to open the door of the study room so that I could work in good conditions.

Abstract

The work presented in this thesis was developed in the framework of the Master in Physics course and the objective was to study, both experimentally and theoretically, vibration modes of C-H bonds in hydrogenated carbon (C:H) films. The samples were grown by Direct Current Hollow Cathode Sputtering (DCHCS) deposition on stainless steel substrates. They mimic the carbon inner coatings of steel tubes used in CERN accelerators where fluxes of high energy particles travel. Then coatings are used to increase the resistance of the tubes. However they degrade with time and researchers at CERN are interested in understanding the role of hydrogen in this process, as well as in quantifying the amount of H atoms incorporated into the coating carbon. The study of vibrational modes will give information concerning the structure and the hydrogen incorporation in the carbon films.

In order to characterize the samples and to study the effect of hydrogen on their properties, several experimental techniques were used in this work, complemented by theoretical modelling. These techniques included Scanning Electron Microscopy (SEM) for the determination of the film thickness, Raman spectroscopy for the study of their structure and evaluation of the ratio of sp^2/sp^3 C-C bonds and also the Fourier Transform Infrared (FTIR) Spectroscopy in both conventional reflection (FTIR-R) mode and the Attenuated Total Internal Reflection (ATR) configuration, with the aim to investigate the effect of hydrogen on the IR spectra in correlation with the amount of H atoms bonded to carbon.

The signatures of the hydrogen forming C-H bonds were also studied theoretically by determining the frequencies and relative intensities of stretching vibration modes using Lagrangian equations of motion and symmetry considerations for certain typical configurations containing a small number of C and H atoms. Theoretical FTIR-R e FTIR-ATR spectra were obtained by using the dielectric function of the C:H material taking into account the contribution of the dipole-active vibration modes and applying the transfer matrix formalism. The calculated spectra were compared with the experimental data, which allowed for the interpretation of the experimentally observed features. In order to quantify the total amount of hydrogen (bonded to carbon or not) the technique of Elastic Recoil Detection Analysis (ERDA) was used.

The Raman scattering spectroscopy results suggest that the studied C:H films are agglomerates of graphite nanocrystals and/or graphene flakes rather than (hydrogenated) amorphous carbon. By the analysis of the Raman spectra, namely, the relative intensity of the characteristic G (graphite) and D (defect) modes and also of the intensity of

the background photoluminescence (which increases with the increase of the percentage of hydrogen in the gas atmosphere used during the film growth) it has been possible to understand the degradation of the carbon films when exposed to hydrogen. The Raman spectra do not reveal hydrogen-related characteristic modes detected by FTIR spectroscopy in the region from 2800 to 3000 cm^{-1}, which means that the effect of the C-H bond stretching vibrations on the electronic susceptibility, for the frequencies corresponding to the light used for Raman scattering excitation in these experiments is too small to be detected.

FTIR spectroscopy, in the conventional reflection mode and especially in the ATR configuration, turned out the most appropriate technique for the study of characteristic C-H vibration modes, allowing for the visualization and quantification of these modes. Unfortunately, because of unknown IR properties of the steel substrates used, the experimental and modelled spectra, although showing the same features, do not allow for global fitting in the whole frequency range studied. However, it has been possible to identify the signature of graphite plasmon, both in the FTIR-R and FTIR-ATR spectra (in the latter case, it is present due to a surface plasmon-polariton mode); it confirms the nano-graphitic nature of the studied C:H films. Moreover, the modelling of the ATR spectra in the range from 2800 to 3000 cm^{-1} is rather convincing and reveals the contribution of five distinct modes corresponding to C-H bonds in different environments. Based on the performed theoretical analysis, these modes have been attributed to (i) hydrogen adsorbed on top of the basal plane of a graphite nanocrystal and/or nano-flake of graphene, (ii) pairs of H atoms linked to zigzag or armchair-type edges and (iii) CH_3 groups formed at Klein edges of the nanocrystals or flakes. All these configurations are characterized by sp^3 bonding of carbon atoms located at the edges and linked to hydrogen. Based on this interpretation, an estimation of the relative concentration of hydrogen in the studied samples has be made.

Resumo

O trabalho aqui apresentado foi desenvolvido no âmbito do Mestrado em Física, tendo como principal objetivo o estudo dos modos de vibração das ligações C-H, do ponto de vista experimental e teórico, em filmes de carbono hidrogenado (C:H). Os filmes foram crescidos pela técnica de Pulverização Catódica Oca de Corrente Continua, DCHCS (Direct Current Hollow Cathode Sputtering) em substratos de aço. As amostras em estudo pretendem reproduzir o efeito do hidrogénio no revestimento interior (carbono em aço) das tubagens por onde passam os feixes altamente energéticos nos aceleradores existentes no CERN. Nas tubagens dos aceleradores usa-se o revestimento em carbono para lhes conferir maior resistência. Com o uso o revestimento interior dos tubos dos feixes no CERN vai-se degradando, estando atualmente os investigadores do CERN interessados neste estudo de forma a desenhar novos revestimentos para os mesmos. Desta forma é fundamental que se perceba o papel do hidrogénio, principal agente da degradação dos tubos, neste processo de degradação. O estudo de modos vibracionais é uma forma não destrutiva de obter informação sobre a estrutura e a incorporação do hidrogénio nestes filmes de carbono.

De forma a caracterizar as amostras e a estudar o efeito do hidrogénio nas suas propriedades, foram utilizadas várias técnicas experimentais, complementadas com estudos teóricos, nomeadamente: SEM (Scanning Electron Microscopy) para determinar a espessura dos filmes de carbono, espectroscopia de difusão Raman para a caraterização estrutural e uma estimativa da razão de carbono com ligações sp^2/sp^3 e ainda espectroscopia de Infravermelho, FTIR (Fourier Transform Infrared Spectroscopy), em modo de reflexão convencional (FTIR-R) e na configuração ATR (Attenuated Total Internal Reflection), com objetivo de estudar as vibrações C-H e relacionar estes modos com a quantidade do hidrogénio ligado ao carbono. A assinatura do hidrogénio ligado ao carbono foi estudada do ponto de vista teórico, determinando as frequências e as intensidades dos modos de vibração do tipo tração/compressão (stretching) associados às ligações C-H, utilizando as equações de movimento, obtidas a partir do Lagrangiano, e considerações de simetria para algumas configurações típicas contendo um número pequeno de átomos C e H. Espectros teóricos de FTIR-R e FTIR-ATR foram também obtidos por modelação, usando a função dielétrica de C:H com a contribuição dos modos vibracionais calculados e aplicando o método de matrizes de transferência, de forma a retirar o máximo de informação relativamente ao efeito do hidrogénio, e comparados com os espectros experimentais. Para a quantificação do hidrogénio ligado e não ligado ao carbono, presente nas amostras foi utilizada a técnica de ERDA (Elastic Recoil

Detection Analysis).

Utilizando a técnica de difusão Raman, verificou-se que os espectros dos filmes em estudo são característicos de aglomerados de folhas de grafite/grafeno e não de carbono amorfo. Pela análise dos espectros Raman, nomeadamente pela intensidade relativa entre os modos caraterísticos de filmes de carbono, denominados como o modo G (grafite) e o modo D (defeitos), pela posição do máximo dos mesmos modos e pela intensidade da banda de luminescência de fundo (que aumenta com o incremento do fluxo de hidrogénio usado no crescimento) foi possível compreender o processo de degradação dos filmes de carbono quando expostos ao hidrogénio. Os espectros Raman das amostras em estudo não apresentam os modos caraterísticos associados às vibrações C-H, revelados pela espectroscopia FTIR na região de 2800 a 3000 cm^{-1}, o que significa que a influência destes modos na porizabilidade eletrónica, para as frequências correspondentes à luz de excitação usada na espectroscopia Raman, é demasiado pequena para ser detetada.

A espectroscopia FTIR, em modo convencional e particularmente em modo ATR, revelou-se a técnica mais adequada para o estudo das vibrações C-H, permitindo visualizar e quantificar vários modos espectrais associados a estas vibrações. Infelizmente, devido ao desconhecimento das propriedades dos substratos de aço usados, os espectros experimentais FTIR-R e os modelados, embora apresentem as mesmas assinaturas, não permitiram efetuar ajustes globais em toda a gama de frequências estudada. No entanto, tornou-se possível identificar a assinatura do plasmão da grafite, quer nos espectros FTIR-R, quer nos FTIR-ATR (na forma do plasmão de superfície), o que confirma a natureza nano-grafítica dos filmes C:H em estudo. Além disso, a modelação dos espectros ATR na região de 2800 a 3000 cm^{-1} é bastante convincente, revelando as contribuições de cinco modos vibracionais de ligações C-H. Com base na análise teórica e dados da literatura, estes modos foram atribuidos a (i) hidrogénio adsorbido em cima do plano basal dos nanocristais da grafite e/ou flocos do grafeno, (ii) pares de átomos H ligados a bordas do tipo "zigzag" ou "armchair" e (iii) grupos CH_3 que se formam nas bordas do tipo Klein dos nanocristais ou flocos. Todas estas configurações são caraterizadas pela ligação sp^3 dos átomos de carbono que ficam nas bordas, ligados a hidrogénio. Com base nesta interpretação foi feita uma estimativa da concentração relativa do hidrogénio nas amostras estudadas.

Contents

1 Introduction **1**
- 1.1 Context and objectives of this work . . . 1
- 1.2 Carbon films . . . 2
- 1.3 Samples growth . . . 4
- 1.4 Introduction to Raman scattering in carbon-related films . . . 6
- 1.5 Introduction to IR spectra of carbon-related films . . . 8
- 1.6 Outline of the thesis . . . 10

2 Experimental techniques used in this work **13**
- 2.1 Raman Spectroscopy . . . 13
- 2.2 Fourier Transform Infra-Red Spectroscopy . . . 15
  - 2.2.1 Basic principles . . . 15
  - 2.2.2 Attenuated Total Reflection Spectroscopy . . . 16
- 2.3 Elastic Recoil Detection Analysis (ERDA) . . . 18
- 2.4 Scanning electron microscopy (SEM) . . . 20

3 Experimental results **23**
- 3.1 Samples' description . . . 23
- 3.2 Raman spectroscopy results . . . 23
- 3.3 FTIR results . . . 26
  - 3.3.1 FTIR reflectance at normal incidence . . . 26
  - 3.3.2 FTIR-ATR . . . 27

4 Modelling of C-H bond stretching vibration modes **29**
- 4.1 Effective stiffness of C-H bond . . . 29
- 4.2 Bond stretching vibrations of a hydrogen atom linked to sp^3-bonded carbon 31
- 4.3 Stretching vibrations of a C-H bond on top of graphite basal plane . . . 39
- 4.4 Bond stretching vibrations of a cluster with two H atoms attached to a graphene sheet . . . 40
- 4.5 Bond stretching vibrations of a C-H on the edge of graphene sheet . . . 42
- 4.6 IR mode assignment . . . 47

5 Modelling of FTIR and ATR spectra **49**
5.1 Theoretical models of reflectance for multilayer samples 49
5.2 Attenuated Total internal Reflection (ATR) spectra 51

6 Discussion of spectroscopy and modelling results **57**
6.1 Raman spectroscopy 57
6.2 IR spectroscopy 58
6.3 Can we estimate the H content from these data? 61

7 Conclusion **63**

A Transfer matrix and Fresnel coefficients **65**

B Processing of experimental data **69**
B.1 Raman spectra 69
B.2 FTIR-ATR spectra 70

List of Figures

1.1 Illustration of the a-C: H film structure having density of 1.7 g/cm^3, 30 at.% hydrogen, 65% sp^2, 20% sp^3 and 15% sp^1. A cluster consisting of rings similar to graphite is evidenced [12]. 3

1.2 Schematic representation of the amorphous carbon coating system at CERN. 4

1.3 (a) Schematic drawing of a general hollow cathode discharge device and (b) photography of the graphite hollow cathode configuration used. . . 5

1.4 (a) Characteristic Raman spectra of some carbon related materials, namely: diamond, graphite, nanocristalline graphite and diamond-like carbon[14] and (b) Scheme illustrating the displacement of the carbon atoms corresponding to the G and D modes of carbon [14]. 7

1.5 Scheme illustrating the displacement of the carbon atoms corresponding to the G and D modes of carbon [14]. 7

2.1 (a) Energy diagram illustration for Rayleigh, Stokes and Anti-Stokes processes, (b) representative spectrum of the Stokes, Rayleigh and Anti-Stokes scattering. 14

2.2 Simple rules illustrating active or inactive vibrations for Raman Scattering and Infra-red absorption [27]. 15

2.3 (a) Scheme of Fourier Spectroscopy, (b) is example of the interferogram function [26]. 16

2.4 Schemes of two experimental methods to measure the surface waves in the attenuated total reflection (a) Otto configuration and (b) Kretschmann configuration. 18

2.5 Schematic illustration of different types of interaction between ion beams and a solid sample [32]. The meaning of the abbreviations are: SIMS - Secondary Ion Mass Spectroscopy; ERDA (or ERD) - Elastic Recoil Detection Analysis; RBS - Rutherford Backscattering Spectrometry; NRA - Nuclear Reaction Analysis; PIXE - Particle induced X-ray emission. . 19

2.6 (a) Schematic illustration of a elastic scattering. Incident ion (mass M_i and energy E_{i0}), atom of the sample (mass M_r) and recoiling ion (mass M_r, energy E_r) and the back scattered ion (mass M_i and energy E_i) and (b) Behaviour of the Kinematic factor for the recoil atoms (Λ) with the mass ratio M_r/M_i and recoil angle (ϕ) [33]. 20
2.7 (a) Schematically representation of the result of the interaction between the electron beam and the matter (b) SEM cross-sectional image of the sample run 3. 21

3.1 Room temperature Raman scattering spectra of the samples. 24
3.2 Peak position of G mode and intensity ratio between D and G modes, from the fit, for all these samples. 25
3.3 Two different groups of Raman spectra of samples growth at: (a) zero and lower concentration of hydrogen and (b) higher concentration of hydrogen in the gas phase. 26
3.4 Reflectance spectra of the samples and substrate. 27
3.5 ATR spectra of all samples. 28

4.1 (a) A fragment of the diamond lattice with one hydrogen atom; (b) scheme showing bond elongation between atoms #2 and #3. 32
4.2 Sheet of graphene with one hydrogen atom on top of the surface, linked to one carbon atom. 39
4.3 (a) Graphene sheet with two hydrogen atoms attached to the top and the bottom of the basal plane; (b) a more detailed diagram of the C-H bonds in the center of the sheet showing the atomic cluster considered explicitly. 41
4.4 Scheme of three types of the edges of grafene: Armchair edge (red), Zigzag edge (blue) and Klein edge (green) [37]. 43
4.5 Scheme of edge of a graphene sheet with (a,b) two and (c) three hydrogen atoms attached to it (sp^2-type bonds are shown thicker). The configuration (a)-(c) correspond to the armchair, zigzag and Klein edges, respectively. 43
4.6 The illustration of the atomic displacements in a cluster containing two hydrogen atoms and one fixed carbon atom, for (a) symmetric and (b) antisymmetric mode; (c) is an auxiliary picture for the calculation of the elongation of the H-H spring. 44
4.7 Representation of (a) symmeric A_1 mode and (b) asymmetric and B_1 mode of a 3-atom cluster. 46
4.8 A 4-atom cluster with 3 hydrogen atoms formed at a Klein edge. The arrows show atomic displacement corresponding to asymmetric (E) modes. 47
4.9 ATR reflectance subtracted from unity, $[1 - R_{ATR}(\omega)]$ C-H modes with baseline at zero intensity, fitted with five Lorentzian fit, of samples 3. . 48
4.10 Diagram showing the assignment of the C-H modes. 48

5.1 Reflectance of free standing C:H films with different thickness. 50
5.2 Calculated reflectance spectra for different thickness of C:H layer in two types of samples: (a) on a 100μm Drude metal slab, (b) SiO_2/Silicon substrate. 51
5.3 Calculated ATR spectra for 250nm free-standing C:H layer in Otto configuration with the gap 250nm and in the Kretschamann configuration. 52
5.4 Calculated ATR spectra and corresponding profiles of transverse electric field across the structure for suspended C:H film in Otto configuration with 200 nm gap (a, b) d=500nm, reduced plasmon damping Γ_p =0.0068 eV (c, d) d=500nm, Γ_p =0.02068 eV (e, f) d=300nm, Γ_p = 0.02068 eV. 53
5.5 Calculated ATR spectra for different thickness of the C:H layer with a Drude metal as substrate. 54
5.6 Calculated ATR spectra of a 200 nm thick C:H layer on a metal substrate for different air gap thicknesses as indicated on he plot (Otto configuration). 55

6.1 Fraction of hydrogen as a function of the slope of the line used to draw baseline to remove PL background in the Raman spectra. 58

A.1 (a) Scheme of a film (thickness d) on a substrate (thickness s) width normal incidence of the light, (b) geometric representation of different layers with choice axes. 65

List of Tables

1.1 Gas mixture composition for each sample. 6
1.2 Assignments of IR frequencies in a-C:H, adapted from [1]. 9

3.1 Amounts of H and N added in gas phase, H and C fractions in the films, and samples' thicknesses. 23
3.2 The position of peaks D and G and ratio of intensity of peaks. 25

5.1 Parameters of the dielectric function for C:H, SiO_2 and Si [39, 40, 41, 42] and frequencies of C-H vibration modes from the experimental data for sample #3. 49

6.1 The results of the fit we have the position, FWHM and area for each peaks. 60
6.2 Relative concentration of hydrogen from IR-ATR spectra. 61

1. Introduction

1.1 Context and objectives of this work

This study was motivated by a practical need for optimization of existing tube linings in modern particle accelerators. The inner walls of the tubes in which the beam travels must be resistant to the impact of high energy particles, photons and other types of radiation [1, 2, 3]. This means that the secondary yield of electrons (SYE) in the inner wall must be very low. In practical means, we should be able to produce an inner layers for which the SYE is of the order of 1%. It is known [4] that by roughening the inner tube surface, for example, using a pulsed laser, a reduction in SEY can be achieved, especially if the inner surface of the steel tube is coated with a carbon film. This carbon coating may be nano-graphitic or amorphous. However, it has been verified at CERN that the presence of hydrogen in the carbon thin films, prepared by magnetron sputtering from graphite targets, has the effect of increasing the SYE of the material [4]. Also, it is known that carbon-based materials are widely used in wear related applications, e.g., bearings, seals, and electrical brushes [5], where the presence of hydrogen in carbon-based materials can significantly affects the friction and wear performance of the material. Thus, the evaluation of the hydrogen content in the carbon-based coatings is very important and can give an important input to solve practical problems. However, this task is not easily fulfilled, especially for small laboratory size samples.

The objective of this work was the study of the vibrational modes associated with C-H bonds of hydrogenated amorphous or nano-graphitic carbon films, both theoretically and experimentally. For this study, Raman scattering and IR spectroscopies were used and the experimental results were supported by theoretical calculations performed using the lattice dynamics model. The practical aim was to explore the possibility of using the information obtained from these studies in order to evaluate the hydrogen contents in the films without using destructive methods.

In this work, the studied a set of hydrogenated carbon films were produced by the deposition technique of Direct Current Hollow Cathode Sputtering (DCHCS) at CERN. These films were produced in order to mimic the real effect of hydrogen on CERN tubes during the usual use. Beyond their characterization by Scanning Electron Microscopy (SEM) and Elastic Recoil Detection Analysis (ERDA), the samples were extensively studied by means of Raman and Fourier Transform Infrared (FTIR) spectroscopes, the latter both in its conventional form (normal incidence reflection) and in the Attenuated

Total Internal Reflection (ATR) configuration. In order to get insight into the nature of observed vibrational modes, especially those related to C-H bonds, lattice dynamics models were developed for small atomic clusters containing hydrogen. These models allow for comparison of the characteristic mode frequencies and get information about the dielectric function of the material. Also, in order to facilitate the comparison with experimental spectra, the transfer matrix method was implemented for the calculation of the IR reflection spectra in both configurations, using as input the dielectric function of composite films in the IR spectral range, which takes into account the dipole-active C-H vibration modes.

1.2 Carbon films

Carbon-related materials have long been the focus of research mainly because of their interesting physical and chemical properties, namely chemical inertness, high hardness and high IR transparency [6]. Moreover, the possibility of sp^2 and sp^3 chemical bonds hybridizations of the carbon atoms allows a properties tailoring, ranging from graphite (only C-sp^2) to diamond (only C-sp^3), passing by NC-graphite and amorphous carbon or even graphene [7, 8], by using the same type of atoms [7, 8]. In the sp^3 configuration, a carbon atom forms four sp^3 orbitals making a strong σ bond to the adjacent atoms. In the sp^2 configuration, the carbon atom forms three sp^2 orbitals forming three σ bonds and the remaining p orbital forms a π bond. The three σ bonds and π bond usually constitute a plane ring in sp^2 clusters.

Among all carbon-based materials, amorphous carbon has been subject of intensive research, mainly related with the aim to achieve and characterize diamond-like-carbon (DLC) materials [9]. These studies are devoted mainly to carbon films produced by Physical Vapour Deposition (PVD r.f. sputtering) or Chemical Vapour Deposition (CVD).

Robertson and O'Reilly [10] have suggested a model for describing amorphous carbon films that consists of sp^2-bonded clusters interconnected by a random network of sp^3-bonded atomic sites. Then, the carbon atoms in amorphous structure (and also nanocrystalline) films can exist in threefold (sp^2) and fourfold (sp^3) bonding coordination, i.e, the films may consist of any mixture of the two bonding types, and the film properties are functions of the sp^2/sp^3 ratio. Under certain deposition conditions nano-crystalline graphite films are produced [11], dominated by sp^2-bonding. Certainly, regimes intermediate between amorphous and nano-graphitic films are also possible. In hydrogenated carbon materials, the hydrogen usually plays an important role in the sp^2/sp^3 ratio. However, even being CH the only bond for hydrogen in carbon films, various combinations of the CH and CC bonds are possible, making the characterization difficult and complicated.

Raman spectroscopy, being a non-destructive technique, is useful for materials characterization and provides information concerning the local bonding, even in amorphous structures. However for the study of carbon-based materials, when using visible light, the π states are resonantly enhanced, whereas the σ states are not, which originates a

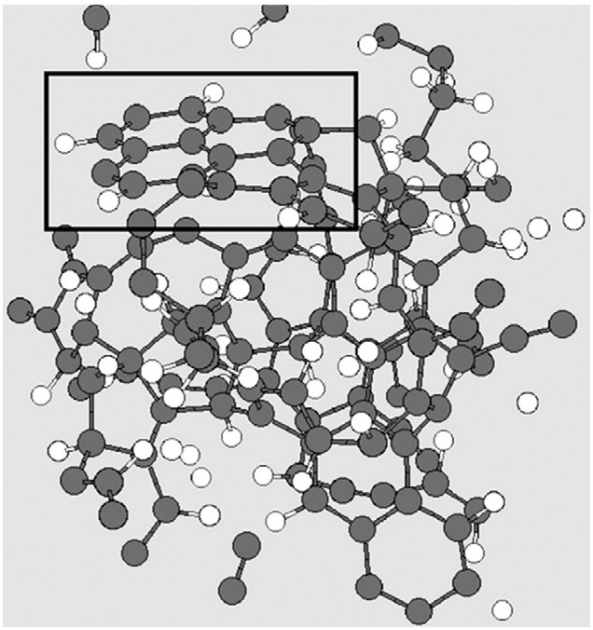

Figure 1.1: Illustration of the a-C: H film structure having density of 1.7 g/cm^3, 30 at.% hydrogen, 65% sp^2, 20% sp^3 and 15% sp^1. A cluster consisting of rings similar to graphite is evidenced [12].

much greater Raman cross section for sp^2 sites, overshadow then the contribution of sp^3 sites [13]. Indeed for this excitation the Raman spectrum is related to the order of the sp^2 sites (not to the sp^2 fraction). Ultra-violet light excites both π and σ states and then it is possible to probe both sp^2 and sp^3 bonds in the material [13].

The first-order Brillouin zone centre mode, a Raman signature of diamond is the presence of a sharp peak at 1332 cm^{-1} with a halfwidth less than 2 cm^{-1}, assigned to T_{2g} symmetry. Graphite is characterized by the presence of a sharp peak at $\approx$ 1580 cm^{-1} (known as G mode or E_{2g} symmetry graphitic mode) [13], whereas disordered graphite presents another peak at $\approx$ 1350 cm^{-1} (known as D band with A_{1g} symmetry, the disorder/defect band) [9]. The G mode is due to the relative motion of sp^2 bonded carbon atoms at chains and rings. The D mode involves phonons near the K point at the Brillouin zone boundary and is Raman-forbidden in perfect graphite, becoming active in the presence of defects. The intensity of this D mode is related with the presence of six-fold aromatic rings. All other types of carbon networks show broad peaks between 1100 and 1600 cm^{-1}. On the other hand, fully amorphous carbon does not present the D peak, since no rings exist. In this way, the intensity ratio of the D and G modes is an important parameter to characterize the carbon films. Indeed the mechanical and optical properties of carbon-based materials depend on the sp^3 content as well on the number and size of clusters with short-range and medium-range ordered sp^2-coordinated carbon atoms.

In the present work we studied samples which represent the tubes used to guide highly energetic beams in the CERN accelerator. The CERN accelerator tubes are

made of steel coated with amorphous carbon film. Beam particles, mainly hydrogen, interact with the surface, originating the degradation of it. To study these samples, several experimental techniques were employed, namely: (i) Raman spectroscopy in order to characterize the vibrational modes of carbon atoms and their changes due to the hydrogen impact, such as the ratio of sp^2/sp^3 bonds; (ii) FTIR spectroscopy in the reflection and ATR configurations, in order to study the CH related bands and then correlate their intensity with the amount of bond hydrogen; (iii) ERDA to determine the total amount of hydrogen, in the samples; (iv) XPS in order to complement the information obtained by the other techniques and also to quantify the sp^2/sp^3 ratio in the samples.

1.3 Samples growth

The studied samples were produced by Direct Current Hollow Cathode Sputtering (DCHCS) technique, illustrated in Figure 1.2.

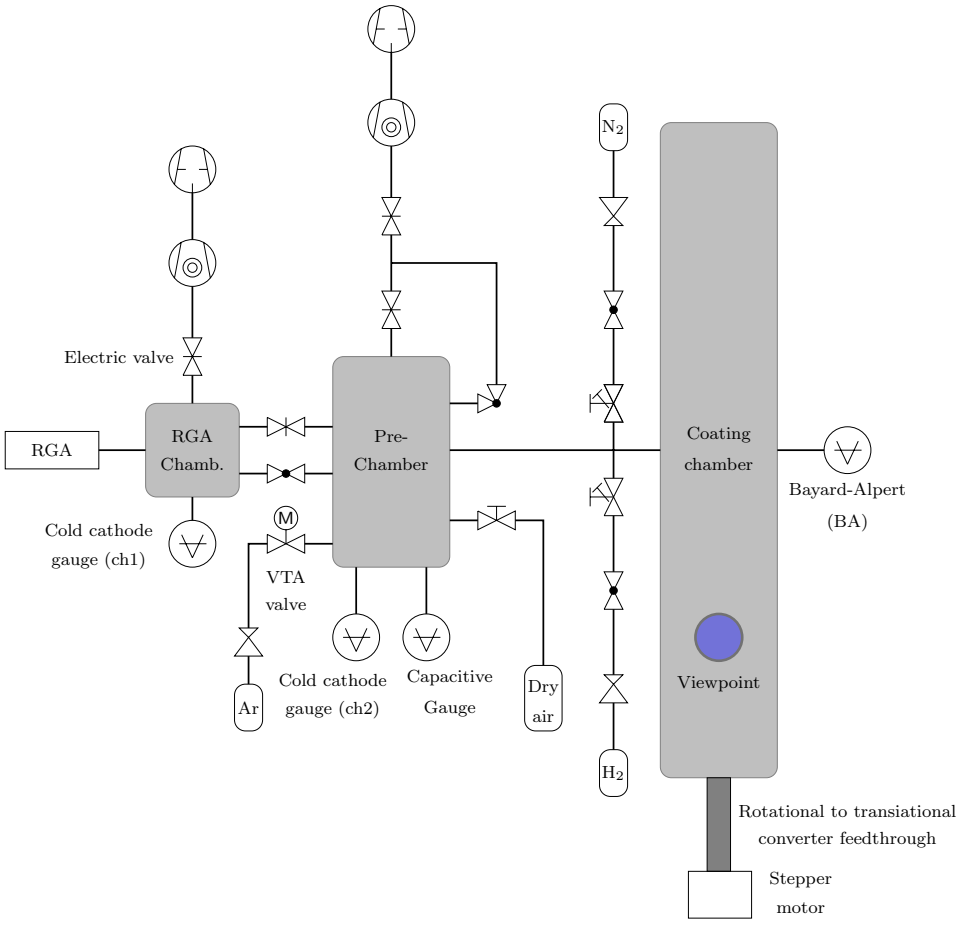

Figure 1.2: Schematic representation of the amorphous carbon coating system at CERN.

In this technique, a cathode of graphite is placed inside the coating chamber. The coating chamber houses a MBB-type SPS liner with open section on the top facing part where 1.5×7 cm stainless steel (StSt) samples are placed. The coating chamber is then connected to a vacuum system containing Argon at low pressure. A voltage of 800V (negative) is applied. The field between the electrode and the mass accelerates free electrons that ionize the Argon and generate more electrons, thus creating a plasma. The argon ions are accelerated by the electrostatic field towards the cathode. They reach the cathode with enough energy to pull carbon atoms from the cathode and they end up projecting onto the substrates, leading to the growth of the film.

In the case of classical glow discharges, electrons are emitted by the cathode, accelerate while passing the cathode drop, ionise the working gas in the negative glow and continue straight towards the anode. In the hollow cathode design the cathode faces another cathode. In this way the electrons are accelerated during the cathode drop until they feel the field of the opposite cathode. This leads to an oscillating movement of the electrons. Figure 1.3a shows schematically the design of a hollow cathode device. The electrons oscillate between the cathodes until they have lost most of their energy and then they move towards the anode. Figure 1.3b shows a photography of the real cathode used in the samples growth.

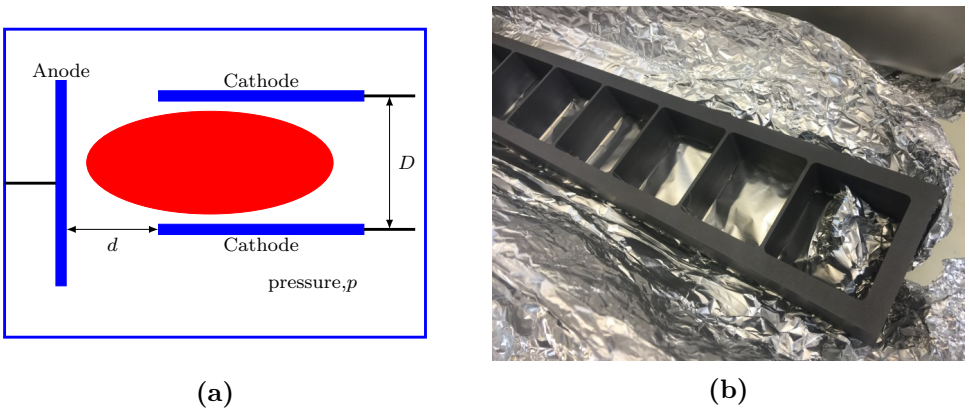

(a) **(b)**

Figure 1.3: (a) Schematic drawing of a general hollow cathode discharge device and (b) photography of the graphite hollow cathode configuration used.

For the growth of the studied samples, besides the inert gas (Ar) it has also been used hydrogen and hydrogen plus nitrogen. Different percentages of added H_2 and/or N_2 were used and Table 1.1 summarizes the gas mixture composition for each sample.

Each sample was grown after 16 hours full-system bakeouts at temperatures ranging from 100 to 200 °C depending on the system components (coating chamber was heated to 200 °C, less heat-tolerant components such as bellows and gate valves 100 °C, other components 150 °C).

Table 1.1: Gas mixture composition for each sample.

Sample	$\%H_2$ added	$\%N_2$ added
1	0	0
2	0	0
3	0.0348	0
5	0.04	0
6	0.1396	0
8	0	0
9	0.13	0.1
10	0.111	0.1

1.4 Introduction to Raman scattering in carbon-related films

Raman scattering, i.e the inelastic scattering of photons by fundamental excitations in molecules or solids, is very usefull for the characterization of carbon-based materials. Most part of the light scattered by a sample is scattered elastically, this process is called Rayleigh scattering. However, a small part is scattered inelastically and this part carries information about the sample. In a Raman scattering process with incident photon energy $\hbar\omega_L$ the scattered photon $\hbar\omega_S$ has lost (Stokes) or gained (anti-Stokes) the energy $\hbar\omega_P$ of an elementary excitation, usually phonon. The Raman scattering is sensitive to probe the local atomic arrangement, meaning that crystalline and amorphous phases or strain can influence the Raman spectra.

As already mentioned, Raman spectra of carbon-related materials show peaks, more or less resolved, between 1100 and 1600 cm^{-1}: known as G mode at $\approx$1580 cm^{-1} and also the D band at $\approx$ 1350 cm^{-1}, as presented in Figure 1.4a for several carbon-related materials. Figure 1.4b presents a scheme illustrating the displacement of the carbon atoms corresponding to the G and D modes shown in the Raman spectra of Figure 1.4a.

Based on the results of numerous Raman studies performed on carbon-based thin films, it is expected a shift on the G peak position associated with a change in the $I(D)/I(G)$ ratio, as illustrated in Figure 1.5. As seen in Figure 1.5, a shift in the G peak position to higher wavenumbers associated with an increase in the $I(D)/I(G)$ ratio can be seen in the left and in the central part of Figure 1.5, corresponding to quite different structures. For a-C:H thin films it is expected a shift of the G peak position to higher wavenumbers, associated with an increase of the intensity ratio between the D and G modes as the material structure becomes more graphitic, which means with the increase of the relative amount of sp^2 bonds. Indeed this is expected because the G mode is due to the stretching vibration of any pair of sp^2 sites in the C=C chain or in the aromatic rings, meaning that the G mode is due to all the sp^2 sites, whereas the D mode corresponds to the breathing vibrations of sp^2 sites, only in the rings (i.e. only the six-fold rings). Since sp^3 sites are only present in the chains, the increase of the D

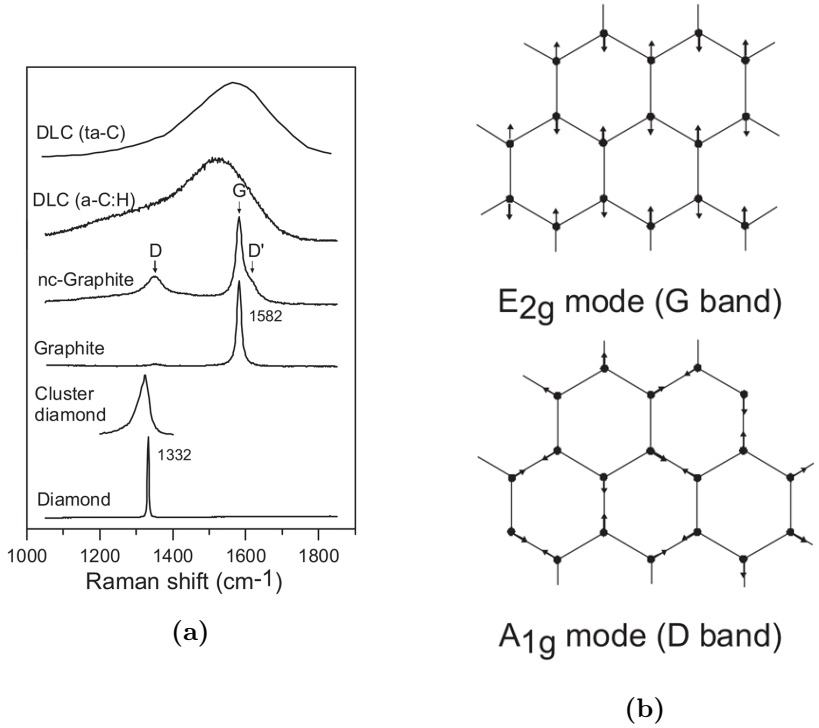

Figure 1.4: (a) Characteristic Raman spectra of some carbon related materials, namely: diamond, graphite, nanocristalline graphite and diamond-like carbon[14] and (b) Scheme illustrating the displacement of the carbon atoms corresponding to the G and D modes of carbon [14].

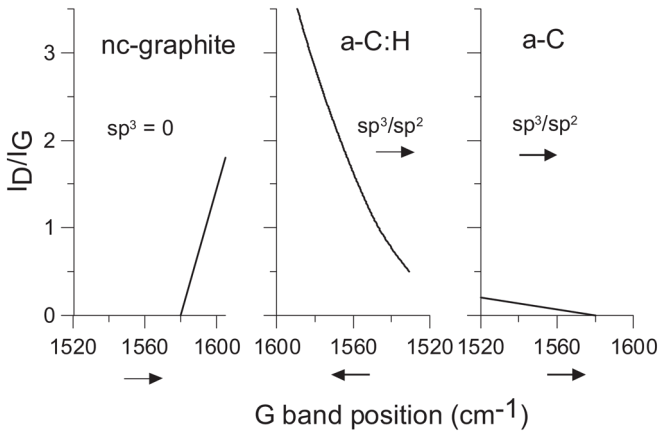

Figure 1.5: Scheme illustrating the displacement of the carbon atoms corresponding to the G and D modes of carbon [14].

mode is related with the decrease of the number of sp^3 sites. Moreover, the full width at half maximum (FWHM) of the Raman modes typically scales with the material

disorder and the shape of the G mode becomes more symmetric as the amount of sp^3 bonds increases. Tuinstra and Koening [15] proposed a relation between the intensity ratio of the D and G modes and the cluster diameter (L_a):

$$\frac{I(D)}{I(G)} = \frac{C(\lambda)}{L_a}, \tag{1.1}$$

where $C(\lambda = 512nm) = 4.4$nm.

Thus the G and D bands contain information on disorder such as the size of aromatic domains and the density of defects. For amorphous carbons (a-C), the $I(D)/I(G)$ can give an indication on the sp^2/sp^3 ratio, and an estimation of the H content for hydrogenated carbons (a-C:H) [16, 17]. The spectroscopic parameters generally used to probe the bonding structure are: the width and the position of the G band, the intensity ratio of the D and G bands, and also the $m/I(G)$ parameter with m being the slope of a superimposed photoluminescence background measured between 800 and 2000 cm^{-1}. Moreover, the shape of the Raman peaks, peak position, and full-half-width are parameters gives information concerning the chemistry and structure of carbon films.

1.5 Introduction to IR spectra of carbon-related films

Infrared spectroscopy is also a non-destructive technique, giving complementary information with respect to the Raman scattering spectroscopy yielding the absorption bands characteristics. It is commonly used to detect molecules possessing polar vibrations accompanied by an oscillating dipole moment [18]. While C-C bonds, in principle, are free from dipole moment, in amorphous carbon films they may show some absorption because of the charge transfer between two carbon atoms with different neighbourhood [10,11], although it is a second order effect compared to the light coupling to C-H vibrations because C-H bonds are indeed polar. Electron charge transfer from hydrogen to carbon is of the order of 0.1e and depends on the particular configuration [19].

The expected absorption bands of a-C:H films are related with C-H stretching vibrations that appear in the 2800-3300 cm^{-1} range, whereas the C-H bending vibrations modes and the C-C mode appear under 2000 cm^{-1}. Bending and wagging modes of C-H bonds are very close to C-C modes [2, 3].

The absorptions related with the C-H stretching modes that appear in the 2800-3000 cm^{-1} range correspond to different bonds, namely the sp^1 ($\equiv$C-H) modes are located at 3300 cm^{-1} , the sp^2 (=C-H) bonds between 2975-3085 cm^{-1} and the sp^3 ($-$C-H) bonds are located between 2850-2955 cm^{-1}, as can seen in more detail in Table 1.2. We may conclude from this table that all C-H modes between 2800 and 2960 cm^{-1} correspond to sp^3-bonded carbon.

Absorption bands at 2855 cm^{-1} and 2920 cm^{-1} are commonly observed in IR spectra of amorphous carbon films and assigned to symmetric and asymmetric stretch modes, respectively, of sp^3-CH_2 configuration [20]. Yet these modes were clearly observed in the spectra of functionalised graphene [21]. Formation of sp^3-bonded carbon atoms with covalently basal phase is now generally accepted by the community [19, 22]. In

Table 1.2: Assignments of IR frequencies in a-C:H, adapted from [1].

wavenumber (cm^{-1})	configuration		Olefinic or aromatic	Symmetric or Antisymmetric
C-H				
3300	sp^1			
3085	sp^2	CH_2	Olefinic	A
3035	sp^2	CH	Aromatic	
2990-3000	sp^2	CH	Olefinic	S
2975	sp^2	CH_2	Aromatic	S
2955	sp^3	CH_3		A
2920	sp^3	CH_2		A
2920	sp^3	CH		
2885	sp^3	CH_3		S
2855	sp^3	CH_2		S
1480	sp^3	CH_3		
1450	sp^3	CH_2		A
1430	sp^2	CH	Aromatic	A
1415	sp^2	CH_3	Olefinic	
1398	sp^3	$(CH_3)_3$		S
1375	sp^3	CH_3		S
C-C				
2180	sp^1			
1640	sp^2		Olefinic	
1580	sp^2		Aromatic	
1515	sp^2/sp^3			
1300-1270	sp^2/sp^3			
1245	sp^2/sp^3			

computational studies on plausible hydrogenation mechanisms it was suggested that the deformation induced by H addition to the sp^2-hybridized lattice atoms leads to increased reactivity in close proximity of these new sp^3-C-H centers, hence favouring an "island-type" hydrogenation, which can take place on both sides of the graphene sheet [23].

The existence of different types of bonding that all may be present in a hydrogen carbon films is a serious difficulty in using IR spectroscopy for evaluation of hydrogen content. This know to work for hydrogenate amorphous silicon, a-Si:H . The number of H atoms per unit volume is obtained by spectral integration of absorption bands related to C-H stretching modes

$$N = \text{const} \int \frac{\alpha(\omega)}{\omega} \mathrm{d}\omega \tag{1.2}$$

where $\alpha(\omega)$ is the absorption coefficient and the "constant" depends on the material

parameters [24]. If works for a-Si:H where all bonds are sp^3. Similar method has been suggested for carbon [1].

Usually the absorption bands are fitted using Gaussian functions to obtain the fraction of the sp^3 bonds, but these bands may be broad and their center deviated, which depends individually on the decomposition of the C-H stretching modes in their bands, which is not unique [25]. However, if the bands are broader and not separated in wavenumber, this fit can not give the information clear as it should be. Furthermore, the oscillator strength of the different C-H bonds is not the same, which makes the determination of the sp^3 amount difficult [1]. Thus, the method of evaluation of hydrogen contents in carbon through integrated absorption is not reliable. Another idea can be to compare the relative intensities of certain absorption modes related to vibration of specific C-H_n configurations that differ only by the number of hydrogen atoms, not by the type of bonding. Then, combining the measured intensity ratio of such modes with statistical relations describing the relative probability of such configurations with different n, may yield the desired evaluation of hydrogen content, at least in relative terms. This idea is explored in the present work.

1.6 Outline of the thesis

The work consisted of experimental and theoretical parts, with the former focused on Raman and IR spectroscopy studies and the latter centred on the development of analytical models for lattice dynamics and IR response of small atomic clusters that are representative of hydrogenated carbon films. The thesis is organized in six chapters and a conclusion section. It contains 37 figures, 7 tables and a bibliographic list consisting of 47 references, and 3 Appendices (A, B.1 and B.2).

The second chapter presents a brief description of the main experimental techniques used in this work, namely, Raman, FTIR and FTIR-ATR spectroscopies, and also the Elastic Recoil Detection Analysis (ERDA) technique, used to determine the film composition (it was performed at the ITN, University of Lisbon). In the third chapter, beyond the samples description and characterization information (such as film thickness and composition obtained by SEM and ERDA, respectively), typical Raman and IR spectra for this carbon-based materials are presented and briefly discussed from the point of view of definition of models to be developed in the subsequent chapter.

The fourth chapter is devoted to analytical models of lattice dynamics of small atomic clusters (containing some carbon atoms and one, two or three hydrogen atoms), based on Lagrange equations of motion, modelling the atoms as masses connected by effective springs. The obtained vibration modes are analysed from the point of view of their symmetry and their contribution to the IR susceptibility of the material is evaluated.

The fifth chapter presents the calculation of IR reflection spectra, in both conventional and ATR configurations, using as input the dielectric function (susceptibility) determined by the dipole-active C-H vibration modes. The calculation is based on the transfer matrix method, which is explained in detail in Appendix.

In the sixth chapter, experimental and theoretical results are compared and discussed, based on the analysis of the observed and calculated C-H vibration modes. This chapter is followed by general conclusions of the work.

2. Experimental techniques used in this work

2.1 Raman Spectroscopy

Raman scattering spectroscopy is an optical technique based on the incidence of a monochromatic electromagnetic radiation with a certain frequency in the material to be analyzed. When light strikes a crystal or molecule, the photons interact with the system through reflection, absorption, transmission, photoluminescence and scattering processes. Through the study of these processes it is possible to determine the electronic and vibrational properties of the material.

In the case of diffused photons, most of them are scattered elastically i.e. with the same energy as the incident photons (Rayleigh scattering). The electronic transitions involved in the light scattering take place between virtual states and the effective cross-section of the interaction is low. In Rayleigh scattering, when electrons fall back to the stationary states, they emit a photon of the same wavelength as the incident photon. However, a small part of the scattered photons, come out with an energy different from the incident photons due to inelastic collisions between photons and atoms, resulting in an increase or decrease in photon energy. This happens because the excited electrons can interact with the atomic network of the solid through the creation or aniquilation of a phonon (quantum of network vibration). When the photon re-emitted by the electron decays into the non-excited state gains energy, it is because anti-Stokes scattering (phonon aniquilation) has occurred, and, on the other hand, when the photon loses energy, the creation of a phonon (Stokes scattering) occurs. Thus, the energy difference between incident light and diffused light is related to the vibrational properties of each material, which means that the Raman frequency is directly related to the frequencies of the elementary excitations (phonons) in the material that gave rise to the scattering. The process of inelastic dispersion of light through a solid or an ensemble molecules is called the Raman effect. The Raman effect was discovered in 1927 by C. V. Raman, who won the Nobel Prize in 1930. Figure 2.1 illustrates the scattering processes in terms of transitions and intensity.

Raman spectroscopy is a powerful experimental technique for the study of structural and vibrational properties of materials, since the phononic spectrum of each solid characterizes it rather comprehensively. The Raman frequency shift is expressed as

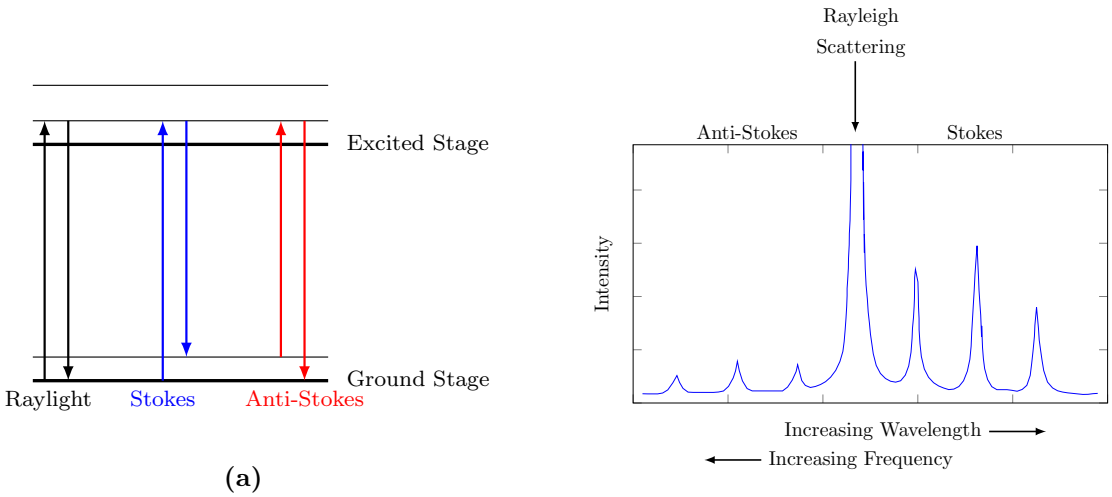

Figure 2.1: (a) Energy diagram illustration for Rayleigh, Stokes and Anti-Stokes processes, (b) representative spectrum of the Stokes, Rayleigh and Anti-Stokes scattering.

follows:

$$\omega_s = \omega_i \pm \omega_0 \tag{2.1}$$

being ω_s the Raman frequency, ω_i the frequency of the incident radiation and ω_0 the frequency of the phonon involved. In the equation the "$-$" sign corresponds to the Stokes process and the "$+$" sign corresponds to the Anti-Stokes process [26].

In the experimental device for Raman spectroscopy, the light scattered by the sample is filtered by a high quality factor band rejection filter, used to remove the laser excitation frequency from the beam, and is then collected by a lens and sent through an optical fiber to the monochromator that scans the beam at wavelengths and sends them to a Charge-Coupled Device (CCD) detector where the optical frequencies present in the scattered beam are recorded. Thus a spectrum of intensities (number of photon counts in the CCD) is created as a function of the frequency of the photon collected. Usually, the Raman deviations are presented in units of wave number (cm^{-1}).

The phonon contributes to Raman scattering only if it changes the polarizability, so not all vibration modes can be seen in the Raman spectra Figure 2.2 shows symmetric and asymmetric stretching or deformations "Q" which leads to a change of the polarizability of the molecule.

The same mode can be Raman and IR-active i.e interact with light indirectly (trough electronic system) and directly; however for crystals the Raman-active phonon modes are IR-silent and vice versa [27].

Molecule					
Vibration					
Change of α with Q	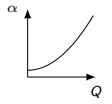	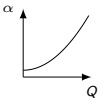	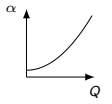	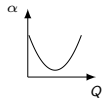	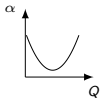
$\frac{\mathrm{d}\alpha}{\mathrm{d}Q}$	$\neq 0$	$\neq 0$	$\neq 0$	$= 0$	$= 0$
Raman active	yes	yes	yes	no	no
Change of $\vec{P}_0$ with Q	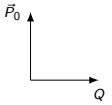	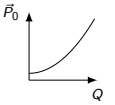	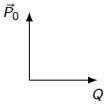	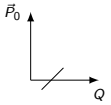	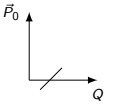
$\frac{\mathrm{d}\vec{P}_0}{\mathrm{d}Q}$	$= 0$	$\neq 0$	$= 0$	$\neq 0$	$\neq 0$
Infraed active	no	yes	no	yes	yes

Figure 2.2: Simple rules illustrating active or inactive vibrations for Raman Scattering and Infra-red absorption [27].

2.2 Fourier Transform Infra-Red Spectroscopy

2.2.1 Basic principles

Infra-Red Spectroscopy is a very popular optical technique, because the majority of materials have absorption modes in this range. In most cases they are related to dipolar atomic vibrations but plasmons and mixed excitations can also contribute. Moreover, this technique is a non-destructive one and the samples usually do not need any special preparation.

From the reflectance or transmittance spectra, recorded in the IR range information about the elementary excitations can be extracted giving information concerning the composition, effective mass, mobility of free electrons, concentration and identification for impurities and defects, thickness of layer or multi-layers and the oscillator strength, and also the phonon frequency and damping. As mentioned in the previous section, the information provided by IR Spectroscopy is complementary to that from Raman spectra concerning the same sample, since some modes are allowed in IR and not in Raman and vice-versa[27]. IR spectroscopy can provide additional information concerning plasmon or coupled phonon-plasmon modes.

The Infra-Red spectra are determined by the dielectric function of the material under study, and also by the size/thickness of the sample, as will be discussed in Section 5.1. In FTIR, the source light is splitted in two beams using a beam splitter. Each of these beams is then reflected by a mirror. One mirror is fixed and the other can move,

changing then the optical pass of the beam: this is the interferemoter principle (as seen in Figure 2.3a). The two reflected beams are then reaching the sample under study an then go to the detector.

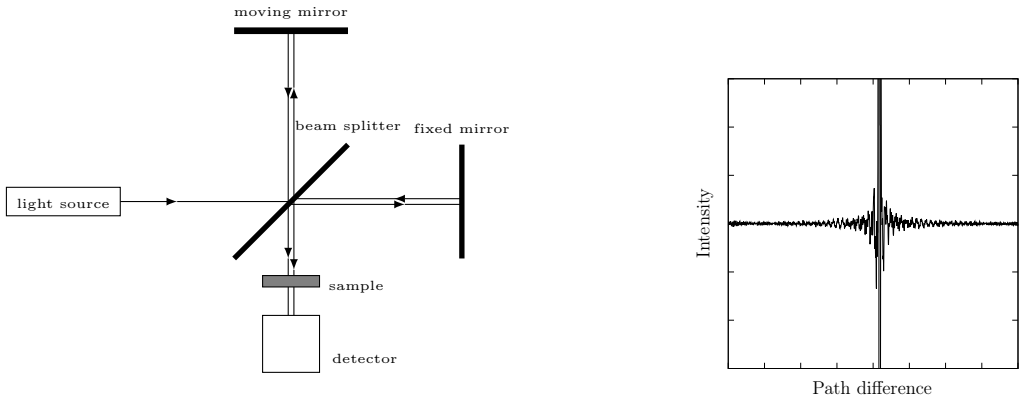

Figure 2.3: (a) Scheme of Fourier Spectroscopy, (b) is example of the interferogram function [26].

The intensity of the sample signal that reaches the detector depends on the difference in the optical path between the two beams. In Figure 2.3b) it is shown a typical interferogram function, where the maximum intensity is achieved for equal optical paths of the 2 beams. The reflectance or transmittance spectra (intensity vs wavenumber) is obtained by calculating the Fourier transform of this interferogram function [26].

2.2.2 Attenuated Total Reflection Spectroscopy

FTIR can also be used in attenuated total internal reflection (ATR) configuration, using a prism (Ge or diamond) facing with the sample. In this configuration an evanescent electromagnetic wave will propagate along the interface between the two media. Only a near-surface region of the structure is probed by the evanescent electromagnetic wave created in this method. The interpretation of ATR spectra is more involved (and interesting) and has been done in this work.

ATR uses a property of total internal reflection resulting in an evanescent wave. A beam of infrared light passes through the ATR crystal in such a way that at least one reflection occurs at the interface crystal/sample. This reflection forms the evanescent wave which extends into the sample. The penetration depth into the sample is low and typically only the top layers of the sample are analysed. It depends on the wavelength of light, the angle of incidence and on the refractive indices of the ATR crystal and the medium being probed [28]. The number of reflections may be varied by varying the angle of incidence. The beam is then collected by a detector.

We must point out that this evanescent wave effect only works if the ATR crystal is made of an optical material having a higher refractive index than the sample, otherwise

light is lost to the sample. Moreover, the penetration of the evanescent wave into the solid sample depends also on the gap between the crystal and the sample (as will be seen in Chapter 5), and the signal to noise ratio depends on the number of reflections and on the total optical length of the light which dampens the intensity. Typical materials for ATR crystals include germanium and diamond, which are cut in the form of a prism.

The evanescent wave emanating from the ATR prism couples only to polar excitations with sufficiently large wavevectors. Examples of such excitations are surface phonon-polaritons (SPPs) for a polar dielectric, or surface plasmon-polaritons for a metal. The necessary condition for the existence of such waves is that (the real parts of) the dielectric constants of the two interfacing media have opposite signs [29].

More precisely the real part of the dielectric functions must obey two conditions:

$$\varepsilon_1 \cdot \varepsilon_2(\omega) < 0 \tag{2.2}$$

and

$$\varepsilon_1 + \varepsilon_2(\omega) < 0 \tag{2.3}$$

The evanescent (surface) waves do not couple directly to propagating ones but it can be achieved in the attenuated total reflection (ATR) configuration. In the geometry of ATR we have a prism on the surface of the sample, with dielectric function much higher than that of the film ($\varepsilon_p > \varepsilon_2(\omega)$) and the angle of incidence of light must be above the critical angle defined as:

$$\theta_c = \arcsin\left(\sqrt{\frac{\varepsilon_\infty}{\varepsilon_p}}\right), \tag{2.4}$$

where ε_∞ is the high-frequency limit of the dielectric function $\varepsilon_2(\omega)$. The component $k_{p,z}$, of the wave vector in the prism is purely imaginary because $k_x > \sqrt{\epsilon_p}\frac{\omega}{c}$,

$$k_{pz} = \sqrt{\varepsilon_p \left(\frac{\omega}{c}\right)^2 - k_{px}^2}. \tag{2.5}$$

Under conditions (2.2) and (2.3), there are surface waves at the surface of the film (see Figure 2.4), with the z-component of wavevector given by:

$$k_{2z} = \sqrt{\varepsilon_2(\omega) \left(\frac{\omega}{c}\right)^2 - k_{2x}^2} \tag{2.6}$$

which is imaginary if $\epsilon_2(\omega)$ is real but usually it is a complex number. If $k_{2x} = k_{px} = \sqrt{\epsilon_p}\left(\frac{\omega}{c}\right)\sin(\theta)$ with θ denoting the incidence angle, the two evanescent waves couple, unless the gap between the prism and the sample (present in the Otto configuration Figure 2.4a) is too big. The gap between the prism and the sample has a strong influence on the coupling intensity. If the gap is small, the resonance is amplified and displaced, due to the damping of the surface wave. The disadvantage of the Otto configuration is the difficulty of controlling the gap value between the prism and the film. An alternative

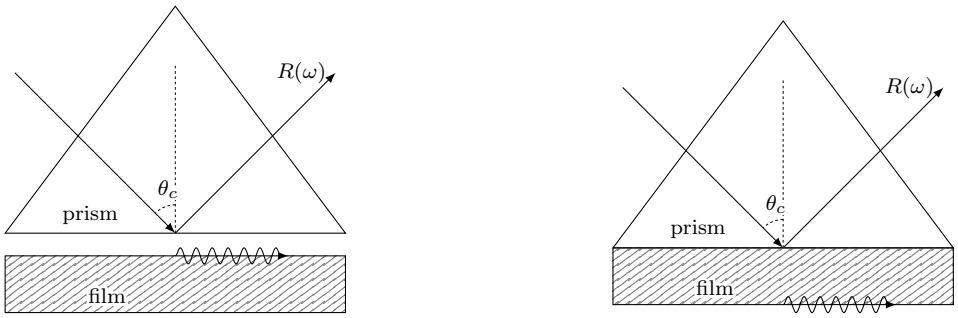

Figure 2.4: Schemes of two experimental methods to measure the surface waves in the attenuated total reflection (a) Otto configuration and (b) Kretschmann configuration.

method is Kretschmann configure (see Figure 2.4b) which is accomplished by depositing film onto the surface of the prism. The light penetrates the entire film and the excitation occurs also the back side of the film (film/air), unless the film absorbs strong [26, 30].

IR spectroscopy in the attenuated total internal reflection configuration was performed with a Golden Gate Single Reflection ATR system (Specac) assembled into a Bruker IFS 66V spectrometer. The infrared beam was directed onto a prism of a monolithic diamond crystal, type IIIA (refractive index $n_p = 2.146$) at an angle of 45°, creating an evanescent wave at the crystal/sample interface. The measurements were performed in air, at room temperature, in the frequency range 500 $\text{cm}^{-1} < \omega <$ 5000 cm^{-1} with a resolution better than 4 cm^{-1}, by using a globar source, a KBr beamsplitter and a DTGS detector with KBr window. The background spectral intensity was acquired with no sample placed on the prism, so that total reflection occurs.

2.3 Elastic Recoil Detection Analysis (ERDA)

Elastic Recoil Detection Analysis (ERDA) was employed to determine the hydrogen content in the samples. ERDA is an ion beam analysis (IBA) method and is based on the detection and identification of recoiling atoms that have been elastically scattered from a sample by an incident heavy ion beam [31].

IBA methods are based on the investigation of the elastic collisions between projectiles and the atoms of the sample or on detection of products of inelastic processes such as electronic excitation and nuclear reactions. The well-known Rutherford Backscattering Spectrometry (RBS) is based on the detection of light projectile ions that were elastically scattered backwards from heavier sample atoms. A typical setup for RBS utilises either beams of protons or He ions, with kinetic energies of several MeV. The energy spectra of the scattered projectiles provide information about the sample. The kinematics of the elastic collision process are such that RBS is capable to detect all the elements that are heavier than the projectile ion with detection limits down to 10^{-12}

at/cm^2 [31].

Elastic recoil detection analysis (ERDA) is a complementary analytical method to RBS. It is based on a principle that is the inverse of RBS. In ERDA heavy projectiles with energies up to several hundreds of MeV collide with sample atoms and knock them out of the sample in the forward direction, where a particle detector is located and measures the energy of the recoiled atoms.

Then ERDA method is devoted to the detection of lighter particles (like hydrogen) from a target sample that were ejected by the incident ions from the beam, whereas RBS method is devoted to the detection of heavier constituents (projectile ions backscattered from the nuclei) in the target sample. Combining these two techniques absolute atomic concentration depth profiles are determined. Figure 2.5 illustrates both methods.

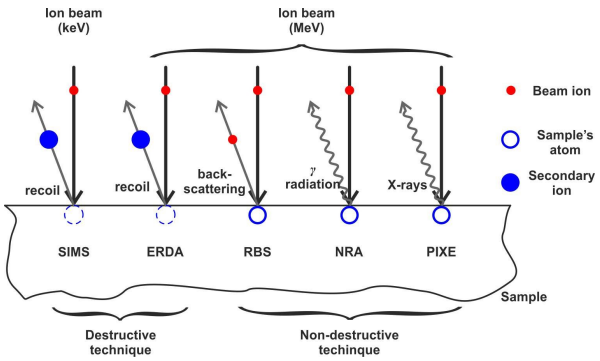

Figure 2.5: Schematic illustration of different types of interaction between ion beams and a solid sample [32]. The meaning of the abbreviations are: SIMS - Secondary Ion Mass Spectroscopy; ERDA (or ERD) - Elastic Recoil Detection Analysis; RBS - Rutherford Backscattering Spectrometry; NRA - Nuclear Reaction Analysis; PIXE - Particle induced X-ray emission.

The advantage of using the ERDA approach is the relatively simple analysis procedure compared to other techniques. Elemental quantification can be expressed as absolute or relative. The absolute concentration indicates the total number of atoms of a certain element present in a sample area and is normally expressed in 10^{-15} at./cm^2 . The relative concentrations of constituent elements of a sample can be directly derived from the respective number of detected events for different elements, weighted according to its corresponding scattering cross-section. The complete sample structure and elemental profiling are normally obtained by the use of simulation programs.

When a beam of ions strikes a solid target, energy is transferred from the incident projectile ion to the target atom. This process is described by kinematic equations of elastic collisions. In a classical two-body elastic collision (Figure 2.6a), the final energy of both particles can be calculated exactly.

In the laboratory co-ordinates, the final energy of a recoiling atom calculated from the energy and momentum conservation laws is given by the following:

$$E_r = \frac{4M_iM_r\cos^2(\phi)}{(M_i+M_r)^2} = \Lambda E_{i0} \tag{2.7}$$

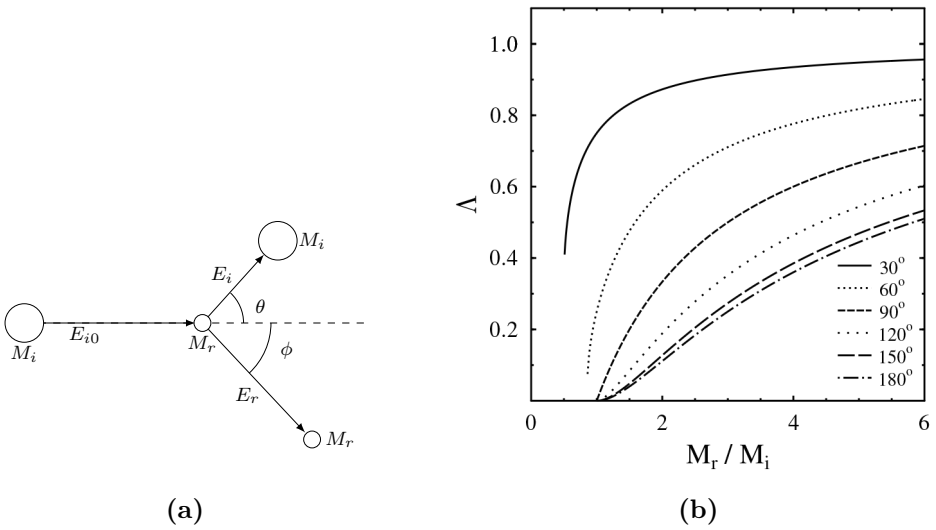

(a) **(b)**

Figure 2.6: (a) Schematic illustration of a elastic scattering. Incident ion (mass M_i and energy E_{i0}), atom of the sample (mass M_r) and recoiling ion (mass M_r, energy E_r) and the back scattered ion (mass M_i and energy E_i) and (b) Behaviour of the Kinematic factor for the recoil atoms (Λ) with the mass ratio M_r/M_i and recoil angle (ϕ) [33].

where ϕ is the recoil angle and Λ is the kinematic factor for the recoil. The kinematic factor for the recoil depends on the masses and on the recoil angle. Figure 2.6b shows how the Kinematic factor for the recoil atoms (Λ) varies with the mass ratio M_r/M_i and with the recoil angle [31].

2.4 Scanning electron microscopy (SEM)

A SEM system is composed of a microscope column, sample chamber, and vacuum system, connected to a computer. The SEM has an electron beam which is accelerated towards the sample, passing by a series of lenses which act to control the diameter of the beam as well as to focus the beam on the sample and a series of apertures which the beam passes through and which affect the properties of the beam. The sample holder allows the control of the sample position (x, y, z) and the sample orientation (tilt, rotation). The selection of the signals that will create the image is done in the beam/sample interaction area. All this is at high vacuum levels.

Figure 2.7a shows schematically what occurs when the beam interacts with the sample: the beam electrons interact with the sample (nucleus and electrons), originating backscattered electrons, secondary electrons, X-rays, Auger electrons and cathadoluminescence. This interaction can be inelastic, resulting in an energy transfer from the beam to the sample atom, releasing an electron from the sample atom (as secondary electron -typically having energy < 50 eV). If the electron beam interacts with the nucleus of the atom sample the interaction is eleastic (change in direction of the electron beam without a significant change in the energy) and if the elastically scattered beam

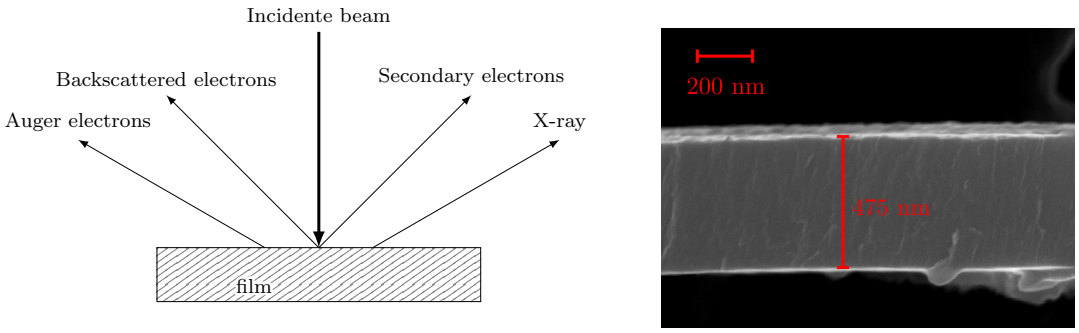

(a) **(b)**

Figure 2.7: (a) Schematically representation of the result of the interaction between the electron beam and the matter (b) SEM cross-sectional image of the sample run 3.

electron is deflected back out of the specimen, the electron is termed a backscattered electron (BSE having energy > 50 eV). The SEM image is constructed based on the secondary electrons and is typically used for morphological characterization, topology characterisation and determination of the film structure.

Although the big possibilities of this technique, in the present work it was used only for determination of the thickness of the studied samples (carbon films).

3. Experimental results

3.1 Samples' description

The samples studied in this work are thin films of hydrogenated carbon grown on stainless steel substrates. They were grown using different gas flows with added hydrogen and (in same cases) nitrogen. Table 3.1 summarises the gases composition used during the samples growth, together with the composition parameters obtained by using ERDA. The film thickness obtained by SEM is also presented. The thicknesses of the samples were measured by cross-section image from SEM (Scanning Electron Microscope), and they range from 345 nm to 690 nm. In the following sections of this chapter we present

Table 3.1: Amounts of H and N added in gas phase, H and C fractions in the films, and samples' thicknesses.

Run	CERN information		ERDA				SEM
			at.%H		at.%C		thickness (nm)
	% H_2 added	%N_2 added	meas.1	meas.2	meas.1	meas.2	
1	0	0	25.27		74.7		690.6
2	0	0	25.64	17.40	74.36	81.85	421.1
3	0.0348	0	20.49	20.19	79.51	78.32	475.0
5	0.04	0	16.29		83.71		421.1
6	0.1396	0	21.46	23.67	78.54	75.58	461.9
8	0	0	18.34		81.66		345.3
9	0.13	0.1	24.22	23.83	75.78	76.16	450.2
10	0.111	0.1	20.50		79.50		504.2

the results obtained by Raman scattering, conventional IR and ATR-IR spectroscopies and discuss the main features of the spectra, while their quantitative analysis is left to Chapter 6.

3.2 Raman spectroscopy results

Raman spectroscopy was performed for all samples, in backscattering geometry, at room temperature, using the 532nm excitation (WiTec Alpha 300R Raman system).

The results are shown in Figure 3.1, where the expected carbon related G and D modes are clearly seen. Moreover, some differences are also seen in the range related to the C-H vibrations (2800-3000cm^{-1}). As already mentioned, relevant information is obtained by the peaks position, FWHM and from the intensity ratio between the G and D modes.

The Raman excitation by visible light is more sensitive to sp^2 bonds than to sp^3 ones because the band gap energy of the state σ-$\sigma*$ is higher than for the state π-$\pi*$ states which needs more energetic photons. The G mode is related to bond-stretching motion of a pair of carbon atoms linked by an sp^2 bond on chains or rings. The D mode is a "braking" mode only existing in the rings. This mode does not exist in perfect graphite and is disorder active. As mentioned in the Introduction from the intensity ratio ($I(D)/I(G)$) information about the disorder and or crystal domains size can be obtained.

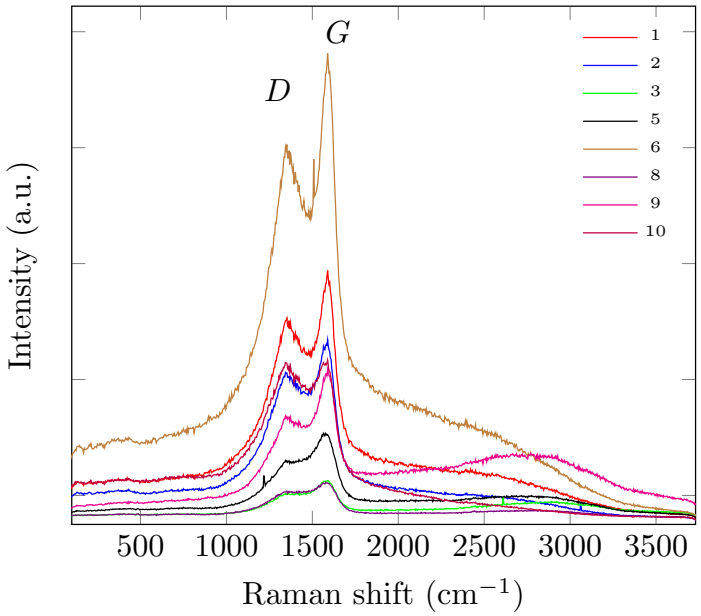

Figure 3.1: Room temperature Raman scattering spectra of the samples.

Figure 3.1 shows the Raman spectroscopy results obtained for samples of Table 3.1. It is seen that the Raman spectra presented in the figure show a background (called luminescence background). Some researchers developed a method to obtain potentially useful information based on this background signal [17]. We removed it for fitting purposes (see Appendix B.1) and also quantified its steepness, which will be discussed in Chapter 6.

The fit of the Raman spectra was performed using Lorentzian functions and the essential parameters were obtained as shown in Table 3.2. From the results in the table it is seen that the peak position of the G mode falls between 1587 and 1594 cm^{-1} (the position of G mode for graphite is 1581 cm^{-1}) and the intensity ratio is between 0.66 to 1.20. Ferrari and Robertson [34] performed a careful Raman study of Carbon-based

Table 3.2: The position of peaks D and G and ratio of intensity of peaks.

run	position D [cm^{-1}]	position G [cm^{-1}]	$I(D)/I(G)$
1	1348	1592	0.88
2	1344	1589	0.92
3	1351	1591	0.66
5	1346	1587	0.67
6	1351	1594	0.88
8	1340	1590	0.77
9	1354	1594	0.72
10	1338	1587	1.20

materials, from graphite to DLC (diamond like carbon), passing by nanocrystalline graphite and amorphous carbon. From this Raman study they concluded that there are three regimes. In the first, corresponding to the amorphyzation of graphite in which the position of the G mode increases and the $I(D)/I(G)$ also increases. In the regime 2 (corresponding to a higher amorphization) the G peak position decreases as also does the $I(D)/I(G)$ ratio. In the third regime (from a-C or a-C:H to DLC) the G peak position increases and the $I(D)/I(G)$ also grows. According to this study, and since the G peak position is higher than in graphite, our samples fall in the first regime, meaning that the samples are composed mainly of NC-graphite.

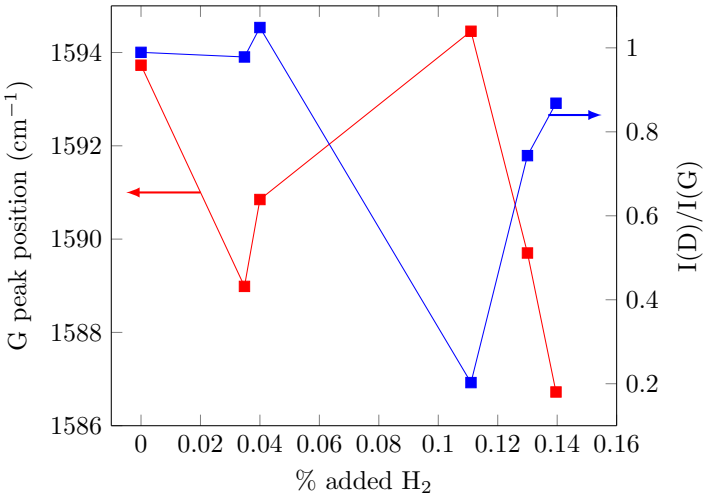

Figure 3.2: Peak position of G mode and intensity ratio between D and G modes, from the fit, for all these samples.

Figure 3.2 shows the G peak position and the intensity ratio ($I(D)/I(G)$) obtained by fitting the Raman spectra, versus the hydrogen percentage used during the growth (Table 3.1). It is seen that, although all the samples present the G mode position at higher Raman shifts than that for graphite, this behaviour and the variation of

$I(D)/I(G)$ with the hydrogen addition present two distinct behaviours: one group in which the G modes shifts to lower wavenumbers, and the intensity ratio almost does not change (samples grown without hydrogen or with hydrogen addition lower than 0.04%) and another group in which along with the shift in the position change the intensity ratio also changes. Indeed for an increase of ω_G a decrease of $I(D)/I(G)$ occurs and vice-versa.

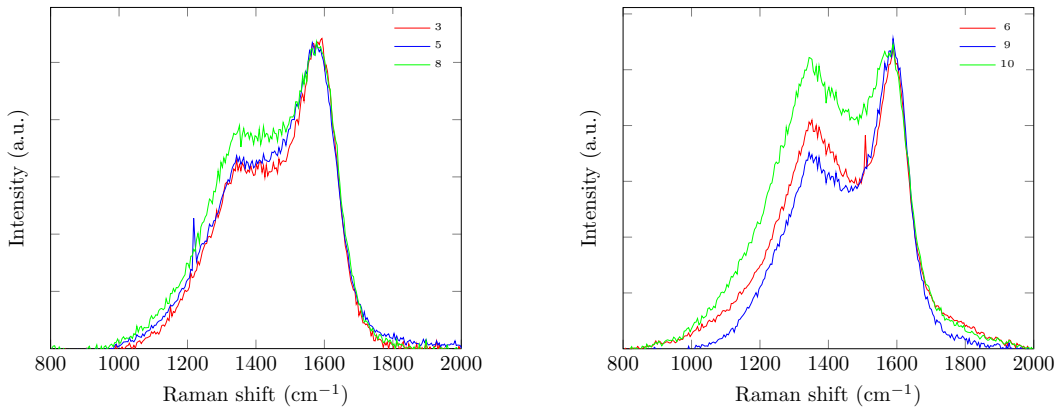

(a) **(b)**

Figure 3.3: Two different groups of Raman spectra of samples growth at: (a) zero and lower concentration of hydrogen and (b) higher concentration of hydrogen in the gas phase.

Trying to better understand this behaviour, Figure 3.3 presents the same Raman spectra but normalized to the G mode intensity (using the Raman spectra of sample 10 as a base). From Figures 3.3a and 3.3b it is seen that the shape and intensity of the D mode is clearly different for the two groups of samples. Indeed, for the samples grown without or little hydrogen, a kind of plateau exist between the G and the D modes and the D mode intensity is low. For the samples grown with high amount of hydrogen, there is a clear evidence of the two Carbon related modes and the D mode intensity clearly high (for sample 10 the D mode intensity is approximately equal to the G mode intensity), indicating a higher disorder of the samples. This disorder probably corresponds to more C-C chains, and/or lower rings size, or even cluster formation. From the shape and intensity ratio of the Raman bands we can conclude that the presence of hydrogen during the sample growth has a strong influence on the D peak intensity (that can be tentatively related with carbon sp^2/sp^3 ratio in the sample).

3.3 FTIR results

3.3.1 FTIR reflectance at normal incidence

All samples were studied by Fourier transform infrared spectroscopy at normal incidence. Stain steel substrate was also measured for comparison. The obtained results

are (below called R-IR spectra) shown in Figure 3.4.

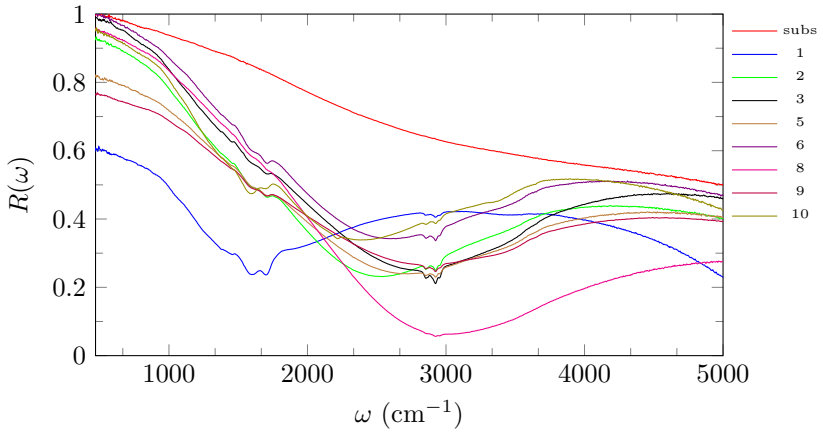

Figure 3.4: Reflectance spectra of the samples and substrate.

From the substrate spectrum shown in Figure 3.4 it can be seen that the substrate must have a capping layer (unknown to us), since the reflection of the substrate is not close to unity, as it should be if the surface was metallic as should be the stain steel [35]. Indeed, for a metallic surface most of the light must be reflected. In this way, the R-IR spectra measured for the samples must also be affected by this unknown coating and the agreement between the theoretical spectra (discussed and presented in Section 5.1) is not as good as it should be. Nevertheless, from the R-IR spectra of the samples it is clear seen the signature of C-C bonds (not present in the substrate) by the observation of modes in the range between 1300 and 1700 cm^{-1}. Moreover, the signature of the C-H bonds is see by the presence of modes in the range around 3000 cm^{-1} [1, 2].

3.3.2 FTIR-ATR

To overcome the effect of the poorly characterised substrate we performed FTIR spectroscopy in the ATR configuration, since in this configuration only a top layer is studied, which means that the substrate will not influence the result. The ATR measurements were also performed in air at room temperature using a germanium prism to create the evanescent wave at the crystal/sample interface. The incidence angle was 45°.

Figure 3.5 shows the obtained ATR spectra. Comparing these results with the previous ones (R-IR spectra, Figure 3.4) it is clearly seen that this configuration not only "removes" the substrate effect but also, and more importantly, highlights the signature of the C-H bonds. Therefore, using the ATR configuration, a more precise information concerning the hydrogen effect on the films can be obtained. By fitting the spectra, the position, FWHM and area of the different spectral bands corresponding to C-H vibrational modes can be obtained (Chapter 5 and Appendix B.2).

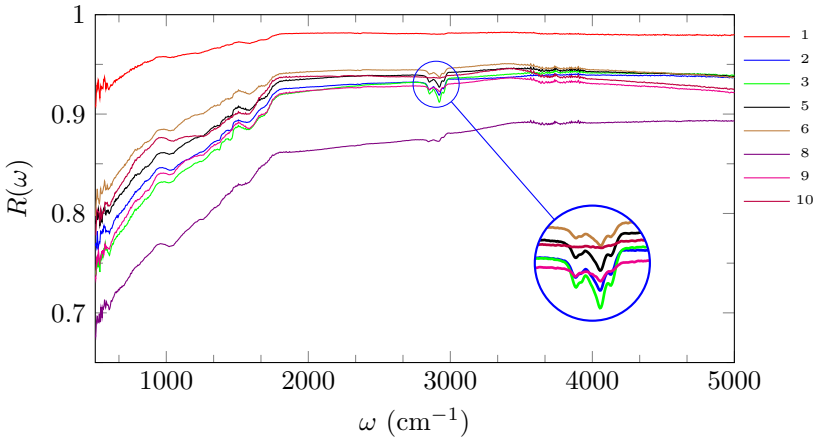

Figure 3.5: ATR spectra of all samples.

4. Modelling of C-H bond stretching vibration modes

4.1 Effective stiffness of C-H bond

This chapter is devoted to theoretical models aimed to describe the hydrogen effect on a carbon-based material in terms of atoms vibrations. The effect of a hydrogen atom inserted in different environments composed of carbon atoms will be studied. Since the hydrogen atom is much lighter than the carbon ones, vibrations involving the covalent C-H stretching bond will appear at significantly higher frequencies compared to C-C bonds [18]. Our experimental results (especially those obtained by IR-ATR spectroscopy, Section 3.3.2) suggest that there exist 3-4 different environment configurations for the C-H bonds, leading to the existence of 3-4 vibrations modes that will appear at slightly different frequencies falling in the 2850-3000 cm^{-1}range. In the theoretical model we will study the lattice dynamics of small clusters of carbon atoms including one and/or two hydrogen atoms and then calculate the frequencies that will characterize the vibrational modes as also their contribution to the IR polarizability.

We start by considering an "isolated" C-H bond and deriving its effective stiffness, taking into account the effect of charge transfer from the hydrogen atom to the carbon atom, which makes this bond partially ionic and, therefore, its stretching vibrations are dipole-active.

We describe the bond between carbon and hydrogen atoms as a spring with a stiffness k_0, which corresponds to the an imaginary situation without considering charge transfer. We further assume that there is a negative charge $(-q_1)$ on the carbon atom and a positive charge $(+q_2)$ on the hydrogen atom. These charges can be unequal in modules if this bond is connected, through the C atom, which have a different carbon environment. From the DFT studies performed for graphene flakes [19], we know that the charge is not localized on the two atoms but distributed between a few neighbour atoms. The Coulomb interaction between these charges affects the bond length and its force constant, parameters that will determine the vibration frequencies. Our aim is to use our experimental data, for these measurable quantities, in order determine the effective stiffness of the bond.

The potential energy of the considered two-atom system is:

$$U = \frac{k_0(\ell - \ell_0)^2}{2} - \frac{1}{4\pi\varepsilon_0}\frac{q_1 q_2}{\ell} \tag{4.1}$$

In the order to calculate the equilibrium length (ℓ_0) and the effective stiffness (k_0) of the "spring" connecting the atoms, we have to know the potential energy U. Then ℓ_0 is found from the following equation:

$$\frac{\partial U}{\partial \ell} = k_0(\ell - \ell_0) - \frac{1}{4\pi\varepsilon_0}\frac{q_1 q_2}{\ell^2} = 0 \tag{4.2}$$

$$\ell^3 - \ell_0\ell^2 - \frac{q_1 q_2}{4\pi\varepsilon_0\ k_0} = 0 \tag{4.3}$$

Equation (4.3) can be re-written as:

$$(\ell - \ell_0)^3 + 2\ell_0(\ell - \ell_0)^2 + \ell_0^2(\ell - \ell_0) - \frac{q_1 q_2}{4\pi\varepsilon_0 k_0} = 0 \tag{4.4}$$

For small length variations, i.e. $|\ell - \ell_0| \ll \ell_0$, the first term of equation (4.4) can be neglected, and then the length variation is given by the following quadratic equation,

$$(\ell - \ell_0)^2 + \frac{\ell_0}{2}(\ell - \ell_0) - \frac{q_1 q_2}{8\pi\varepsilon_0\ell_0 k_0} = 0; \tag{4.5}$$

$$\ell - \ell_0 = -\frac{\ell_0}{4} + \sqrt{\frac{\ell_0^2}{16} + \frac{q_1 q_2}{2\pi\varepsilon_0\ell_0 k_0}} \tag{4.6}$$

(we take the sign "+" because $\ell = \ell_0$ for $q_1 = q_2 = 0$).

Therefore

$$\ell - \ell_0 = \frac{\ell_0}{4}\left[-1 + \sqrt{1 + \frac{8q_1 q_2}{\pi\varepsilon_0\ell_0^3 k_0}}\right] \tag{4.7}$$

and the "new" (true) equilibrium length of the bond,

$$\ell_{eq} = \ell_0\left[\frac{3}{4} + \frac{1}{4}\sqrt{1 + \frac{8q_1 q_2}{\pi\varepsilon_0\ell_0^3 k_0}}\right] \simeq \ell_0 + \frac{q_1 q_2}{4\pi\varepsilon_0\ell_0^3 k_0} \tag{4.8}$$

since $q_1 q_2 < 0$, $\ell_{eq} < \ell_0$.

It is now possible to determine the effective stiffness of the bond by expanding equation (4.1) in the vicinity of $\ell = \ell_{eq}$ and assuming $\ell = \ell_{eq} + \triangle\ \ell$; $\triangle\ \ell \ll \ell_{eq}$:

$$U = \frac{k_0(\ell_{eq} - \ell_0 + \triangle\ \ell)^2}{2} + \frac{q_1 q_2}{4\pi\varepsilon_0(\ell_{eq} + \triangle\ \ell)} = \tag{4.9}$$

$$= \frac{k_0(\ell_{eq} - \ell_0)^2}{2} + k_0(\ell_{eq} - \ell_0)\ \triangle\ \ell + \frac{k_0\ \triangle\ \ell^2}{2} + \frac{q_1 q_2}{4\pi\varepsilon_0\ell_{eq}} - \frac{q_1 q_2\ \triangle\ \ell}{4\pi\varepsilon_0\ell_{eq}^2} + \frac{q_1 q_2\ \triangle\ \ell^2}{4\pi\varepsilon_0\ell_{eq}^3} \tag{4.10}$$

The linear terms cancel because $\triangle\ \ell = 0$ corresponds to equilibrium and the potential energy becomes:

$$U = const + \frac{1}{2}\left(k_0 + \frac{2q_1q_2}{4\pi\varepsilon_0\ell_{eq}^3}\right)(\triangle\ \ell)^2. \tag{4.11}$$

Thus, the effective stiffness is given by:

$$k' = k_0 - \frac{2q_1q_2}{4\pi\varepsilon_0\ell_{eq}^3} \simeq k_0 - \frac{2q_1q_2}{4\pi\varepsilon_0\ell_0^3}\left(1 - \frac{3q_1q_2}{4\pi\varepsilon_0\ell_0^3k_0}\right) \tag{4.12}$$

and the vibrational frequency of this bond is:

$$\omega_0 = \sqrt{\frac{k'}{\mu}} \tag{4.13}$$

where $\mu = \frac{mM}{m+M}$ is the effective mass. In this way, if experimentally we obtain the vibrational frequency (ω_0), it is possible to calculate the effective stiffness (k'), using equation (4.13). Also, the equilibrium bond length (4.8) for a molecule, in principle, can be measured independently. However, based only in two parameters obtained from the experimental measurements (the equilibrium bond length and the stretching vibration frequency), it is not possible to obtain information about all the parameters used in this model, namely: k_0, ℓ_0, q_1 and q_2. In principle, based on the absorption spectrum, the charge product can be extracted from the oscillator strength, since $q_1q_2\omega_0^2/\mu$.

However, we can also use DFT calculated results for the charges determination. They are computed to reproduce electrostatic potentials generated by the molecule. For instance, for a graphene flake with a hydrogen atom chemisorbed on the basal plane the charge is $q_1 = +0.12$e for the H atom, while the charge on the C atom bonded to it is $q_2 = -0.06$e [19]. The reminding negative charge, $-(q_1 + q_2) = -0.06$e, is not localized but we may think that it is distributed over the nearest neighbours of the C atom bonded to hydrogen. Also, the DFT calculations yield ℓ_{eq} values, which depend considerably upon the environment configuration of the C-H bond. The effective stiffness of the C-H bond in the diatomic molecule CH is evaluated as $k' \simeq 4.5\cdot10^{-8}$N/Å from the stretching vibration frequency $\omega_0 \simeq 2862\text{cm}^{-1}$ [18].

4.2 Bond stretching vibrations of a hydrogen atom linked to sp^3-bonded carbon

We begin by considering a fragment of the diamond lattice with a hydrogen atom replacing one carbon atom. The bond between carbon and hydrogen atoms has the effective stiffness k' determined in Section 4.1. The other bonds are modelled by springs with a different stiffness k.

In this study we only consider the C-H vibration along z direction (see in Figure 4.1). The displacements of the two (H and C) atoms along z can be writen in terms of normal coordinates $u_{1,2}$:

$$u_1 = \sqrt{m}\left(z_1 - z_1^{(0)}\right); \tag{4.14}$$

$$u_2 = \sqrt{M}\left(z_2 - z_2^{(0)}\right), \tag{4.15}$$

where $z_{1,2}^{(0)}$ denote the equilibrium positions of two atoms.

However, the neighbouring carbon atoms number 3, 4 and 5 can vibrate along another (not z) direction and we denote their displacement vector multiplied by $\sqrt{M}$ as $\vec{u_i}$ $(i = 3, 4, 5)$. Let´s us consider the situation schematically represented in Figure

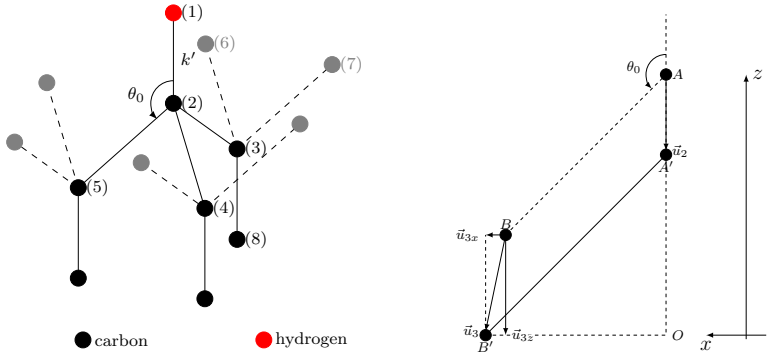

(a) **(b)**

Figure 4.1: (a) A fragment of the diamond lattice with one hydrogen atom; (b) scheme showing bond elongation between atoms #2 and #3.

4.1a , focusing on the C-C vibration of the carbon atom which is also bonded to the hydrogen. According to the scheme presented in Figure 4.1b, the displacement can be written as:

$$A'O = \ell\cos(\pi - \theta_0) - u_2 + u_{3z}, \tag{4.16}$$

$$B'O = \ell\sin(\pi - \theta_0) + u_{3x}. \tag{4.17}$$

Therefore the length variation of the stretched bond is:

$$\triangle\ \ell_{23} = \sqrt{(A'O)^2 + (B'O)^2} - l \tag{4.18}$$

$$= \sqrt{\ell^2 + 2\ell\cos(\pi - \theta_0)(u_{3z} - u_2) + 2\ell u_{3x}\sin(\pi - \theta_0)} - \ell, \tag{4.19}$$

$$\simeq u_2' - u_3' \tag{4.20}$$

where $u_{2,3}'$ represent the projection of the corresponding atomic displacements onto the (undeformed) bond 3-2. For u_2', can be written as:

$$u_2' = u_2\cos(\theta_0) \equiv \sqrt{\gamma}u_2; \tag{4.21}$$

$$u_3' = u_{3x}\sin(\theta_0) - u_{3z}\cos(\theta_0), \tag{4.22}$$

where $\gamma^2 = \cos(\theta_0)$.

The kinetic energy of the system is:

$$T = \frac{1}{2}\sum_{i=1}^{5} \dot{u}_i^2. \tag{4.23}$$

Considering the bonds between atoms as simple springs, the total potential energy is then given by:

$$\begin{aligned} U_{elastic} = & \frac{k'}{2}\left(\frac{u_2}{\sqrt{M}} - \frac{u_1}{\sqrt{m}}\right)^2 \\ & + \frac{k}{2M}\left[(u_2' - u_3')^2 + (u_6' - u_3')^2 f_{63} + (u_7' - u_3')^2 f_{73} + (u_8' - u_3')^2 f_{83}\right] \\ & + \dots \end{aligned} \tag{4.24}$$

The Lagrange function is the difference between the kinetic and potential energies and is given by:

$$\begin{aligned} \mathcal{L} = & \frac{1}{2}\sum_{i=1}^{5} \dot{u}_i^2 - \frac{k'}{2}\left(\frac{u_2}{\sqrt{M}} - \frac{u_1}{\sqrt{m}}\right)^2 \\ & - \frac{k}{2M}\left[(u_2' - u_3')^2 + (u_6' - u_3')^2 f_{63} + (u_7' - u_3')^2 f_{73} + (u_8' - u_3')^2 f_{83}\right] \\ & - \dots \end{aligned} \tag{4.25}$$

where u_i' always means projection onto bond 2-3 and the factors f_{63}, f_{73}, f_{83}, take into account the relative orientation of the 3-6, 3-7 and 3-8 bonds, respectively, with respect to the 2-3 one. Equations (4.24) and (4.25) include similar terms but for atoms 4 and 5 (and not only atoms 3), and also for more remote atoms that will not be considered.

From (4.25) the equations of motion can be derived:

$$\frac{d}{dt}\left(\frac{\partial \mathcal{L}}{\partial \dot{u}_i}\right) - \frac{\partial \mathcal{L}}{\partial u_i} = 0. \tag{4.26}$$

For atoms 1, 2 and 3 they can be explicitly presented as:

$$\begin{cases} \ddot{u}_1 + \frac{k'}{\sqrt{m}}\left(\frac{u_1}{\sqrt{m}} - \frac{u_2}{\sqrt{M}}\right) = 0; \\ \ddot{u}_2 + \frac{k'}{m}\left(\frac{u_2}{\sqrt{M}} - \frac{u_1}{\sqrt{m}}\right) + \frac{k}{M}\left[3\gamma u_2 - \sqrt{\gamma}(u_3' + u_4' + u_5')\right] = 0; \\ \ddot{u}_3' + \frac{k}{M}\left[(u_3' - \sqrt{\gamma}u_2) + (u_3' - u_6')f_{63} + (u_3' - u_7')f_{73} + (u_3' - u_8')f_{83}\right] = 0; \\ \dots \end{cases} \tag{4.27}$$

and, in a similar way for the atoms 4 and 5.

We search solutions of equations (4.27) in the form:

$$u_i = \mathrm{Re}(b_i e^{-i\omega t}) \tag{4.28}$$

where b_i are complex amplitudes. Substituting (4.28) into (4.27) yields:

$$\begin{cases} \left(\frac{k'}{m} - \omega^2\right) b_1 - \frac{k'}{\sqrt{mM}} b_2 = 0; \\ -\frac{k'}{\sqrt{mM}} b_1 + \left(\frac{k'+3\gamma k}{M} - \omega^2\right) b_2 - \frac{\gamma k}{M} b_3 - \frac{\gamma k}{M} b_4 - \frac{\gamma k}{M} b_5 = 0; \\ -\frac{\gamma k}{M} b_2 + \left(\frac{\gamma k}{M}(1 + f_{63} + f_{73} + f_{83}) - \omega^2\right) b_3 + \frac{\sqrt{\gamma} k f_{63}}{M} b_6 + \frac{\sqrt{\gamma} k f_{73}}{M} b_7 + \frac{\sqrt{\gamma} k f_{83}}{M} b_8 = 0; \\ \ldots \end{cases} \tag{4.29}$$

We can use symmetry arguments to simplify the system of equations (4.29). The 5 atom cluster ($i = 1 - 5$) that we are going to consider explicitly has point symmetry group C_{3v} containing the 3rd order rotation axis along z and three vertical symmetry planes. The irreducible representations of this group are called A_1, A_2 and E; the latter is two-dimensional and represents two fold degenerate modes.The representations A_1 and E correspond to dipole-active modes [18]. These modes/representations, in the present work will be designated as:

(i) Symmetric (A_1 representation), $b_3 = b_4 = b_5$;

(ii) Asymmetric (E representation, 2-fold degenerate), with $b_3 = e^{i\frac{2\pi}{3}} A_4 = e^{i\frac{4\pi}{3}} A_5$ (rotation introduces a phase shift of $\pm\frac{2\pi}{3}$), so that

$$u'_3 + u'_4 + u'_5 = 0. \tag{4.30}$$

(i) Symmetric modes

Considering $b_3 = b_4 = b_5$ and neglecting the terms containing f_{ij} factors in the equations (4.29), the dynamical matrix is:

$$\hat{D}_S = \begin{bmatrix} \frac{k'}{m} & -\frac{k'}{\sqrt{mM}} & 0 \\ -\frac{k'}{\sqrt{mM}} & \frac{k'+3\gamma k}{M} & -\frac{3\gamma k}{M} \\ 0 & -\frac{3\gamma k}{M} & \frac{3\gamma k}{M} \end{bmatrix}. \tag{4.31}$$

The dynamical matrix (that allows to write the equations of the motion in a compact form[1]) is composed of the 2nd derivatives of the potential energy with respect to the normal coordinates.

[1]The compact form of the (4.29) is $\hat{D}|u\rangle = \omega^2|u\rangle$, $|u\rangle$ represents a column vector composed of normal coordinated u'_i with $i = 1 - 5$. By virtue of symmetry, it can be reduced to just 3 entrées.

The last line in matrix (4.31) represents the sum of 3 equations for $i = 3, 4, 5$, so the corresponding kinetic energy term must be taken as $-3b_3\omega^2$. The eigenfrequencies are obtained from the equation:

$$\left|\hat{D}_S - \omega^2 \hat{I}'\right| = 0 \tag{4.32}$$

where

$$\hat{I}' = \begin{bmatrix} 1 & 0 & 0 \\ 0 & 1 & 0 \\ 0 & 0 & 3 \end{bmatrix}. \tag{4.33}$$

Equation (4.32) reduces to:

$$\omega^6 - \omega^4 \left(\frac{k'}{\mu} + \frac{4\gamma k}{M}\right) + \omega^2 \left(\frac{4\gamma k' k}{mM} + \frac{\gamma k' k}{M^2}\right) = 0. \tag{4.34}$$

There is one translational mode, $\omega^2 = 0$, and two non-trivial ones, given by::

$$\begin{aligned} \omega^2_{2,3} &= \frac{1}{2}\left[\left(\frac{k'}{\mu} + \frac{4\gamma k}{M}\right) \pm \sqrt{\left(\frac{k'}{\mu} + \frac{4\gamma k}{M}\right)^2 - 4\left(\frac{4\gamma k' k}{mM} + \frac{\gamma k' k}{M^2}\right)}\right] \\ &= \frac{1}{2}\left[\left(\frac{k'}{\mu} + \frac{4\gamma k}{M}\right) \pm \sqrt{\left(\frac{k'}{\mu} - \frac{4\gamma k}{M}\right)^2 + \frac{12\gamma k' k}{M^2}}\right]. \end{aligned} \tag{4.35}$$

The high frequency mode ("+") is the dipole-active one and its frequency is close to $\omega_0 = \frac{k'}{\mu}$, characteristic of an isolated C-H bond. Taking into account that $m, \mu \ll M$ and keeping the lowest order corrections to the main term, for the other ("−") mode we get:

$$\omega^2_3 \simeq \frac{k'}{\mu} + \frac{3\gamma k \mu}{M^2} + 12\frac{\gamma^2 k^2 \mu^2}{k' M^2}. \tag{4.36}$$

(ii) Asymmetric modes

The dynamical matrix is:

$$\hat{D}_A = \begin{bmatrix} \frac{k'}{m} & -\frac{k'}{\sqrt{mM}} \\ -\frac{k'}{\sqrt{mM}} & \frac{k' - 3\gamma k}{M} \end{bmatrix} \tag{4.37}$$

and the eigenfrequencies are obtained by the equation:

$$\omega^4 - \omega^2 \left(\frac{k'}{\mu} + \frac{3\gamma}{M}\right) + \frac{3\gamma k' k}{mM} = 0. \tag{4.38}$$

There are two solutions:

$$\begin{aligned}\omega_{4,5}^2 &= \frac{1}{2}\left[\left(\frac{k'}{\mu}+\frac{3\gamma k}{M}\right) \pm \sqrt{\left(\frac{k'}{\mu}+\frac{3\gamma k}{M}\right)^2 - \frac{12\gamma k k'}{mM}}\right] \\ &= \frac{1}{2}\left[\left(\frac{k'}{\mu}+\frac{3\gamma k}{M}\right) \pm \sqrt{\left(\frac{k'}{\mu}-\frac{3\gamma k}{M}\right)^2 + \frac{12\gamma k k'}{M^2}}\right].\end{aligned} \tag{4.39}$$

Using the same aproximation as before (leading to (4.35)), for the high frequency asymmetric mode we have:

$$\omega_5^2 = \frac{k'}{\mu} + \frac{3\gamma k\mu}{M^2} + 9\frac{\gamma^2 k^2 \mu^2}{k' M^2}. \tag{4.40}$$

Comparing equations (4.40) and (4.36), it is clear that ω_5 is aproximatelly iqual to ω_3, however, $\omega_5 < \omega_3$. This mode is two-fold degenerate because clockwise or anticlockwise rotations are possible:

$$b_1 = b_2 e^{\pm\frac{2\pi}{3}} = b_2 e^{\pm\frac{4\pi}{3}}, \tag{4.41}$$

which generate the two-dimensional representation E. From now on, we will identify these two modes as symmetric (S) and asymmetric (A). Then, $\omega_S = \omega_3$ [equation (4.36)] and $\omega_A = \omega_5$ [equation (4.40)].

The eigenvectors

From Eq. (4.29) we obtain:

$$\beta = \frac{u_2}{u_1} = \frac{\frac{k'}{m} - \omega^2}{\frac{k'}{\sqrt{mM}}} = \sqrt{\frac{M}{m}}\left[1 - \frac{\omega^2}{\omega_0^2}\left(1 - \frac{m}{M}\right)\right], \tag{4.42}$$

which is valid for either symmetric or asymmetric mode [(4.36),(4.40)]. Substituting the corresponding frequency in equation (4.42), the obtained β parameter is:

$$\beta = -\sqrt{\frac{m}{M}} + \frac{3\gamma k}{k'}\left(\frac{m}{M}\right)\left(\frac{\mu}{M}\right) + \cdots \simeq -\sqrt{\frac{m}{M}}. \tag{4.43}$$

However, using equation (4.29) (corresponding to the symmetric mode), the result is different:

$$\delta = \frac{u_3}{u_1} = \frac{\beta}{1 - \frac{M\omega}{\gamma k}}. \qquad\qquad \delta \ll |\beta|. \tag{4.44}$$

The normalized eigenvector, for the symmetric mode, is:

$$|u\rangle_S = \frac{1}{\sqrt{1+\beta^2+3\delta^2}}\begin{bmatrix}1\\ \beta\\ \delta\\ \delta\\ \delta\end{bmatrix}. \tag{4.45}$$

and for the asymmetric modes we have:

$$|u\rangle_A^{\pm} = \frac{1}{\sqrt{1+\beta^2+3\delta_A^2}} \begin{bmatrix} 1 \\ \beta \\ \delta_A \\ \delta_A e^{\pm i\frac{2\pi}{3}} \\ \delta_A e^{\pm i\frac{4\pi}{3}} \end{bmatrix}. \tag{4.46}$$

Using this model we can not determine the parameter δ_A because u_3', u_4' and u_5' were dropped off. However, we are sure that $|\delta_A| \ll |\beta|$ because carbon atoms cannot vibrate at such a high frequency.

Since in our model only atoms 1 and 2 have a considerable electric charge and their vibration amplitudes, for either ω_S or ω_A, are much larger than for all other atoms, we will consider equal eigenvectors (because $\omega_S \simeq \omega_A$),

$$|u\rangle_{A,S} = \frac{1}{\sqrt{1+\beta^2}} \begin{bmatrix} 1 \\ \beta \end{bmatrix}. \tag{4.47}$$

Polarisability of C-H vibration modes

In order to calculated the polarisability associated with dipole-active vibration modes, we consider an external force acting on the charged atoms, with the following potential energy:

$$U_{driving} = -qE(z_1 - z_2) \tag{4.48}$$

for simplicity, we assume $q_1 \simeq -q_2 = q$.

Considering this potential energy the equation of motion (4.32) change to:

$$\left(\hat{D} - \omega^2 \hat{I}\right)|u_i\rangle = |R\rangle, \tag{4.49}$$

where

$$|R\rangle = \begin{bmatrix} \frac{qE}{\sqrt{m}} \\ -\frac{qE}{\sqrt{M}} \end{bmatrix} \equiv \hat{Q} \begin{bmatrix} 1 \\ 1 \end{bmatrix} E \tag{4.50}$$

and $\hat{Q}$ is a "charge matrix":

$$\hat{Q} = \begin{bmatrix} \frac{q}{\sqrt{m}} & 0 \\ 0 & -\frac{q}{\sqrt{M}} \end{bmatrix}. \tag{4.51}$$

The amplitude of the forced vibration is then given by:

$$|u_f\rangle = \left(\hat{D} - \omega^2 \hat{I}\right)^{-1} |R\rangle = \hat{G}|R\rangle \tag{4.52}$$

where $\hat{G}$ ys the Green's function.

We can used the Green's function expansion in terms of eigen-modes and eigenvectors,

$$\hat{G} = \sum_i \frac{|u_i\rangle\langle u_i|}{\omega_i^2 - \omega^2} \tag{4.53}$$

and replace in equation (4.52):

$$|u_f\rangle = \sum_i \frac{|u_i\rangle\langle u_i|}{\omega_i^2 - \omega^2}|R\rangle = \sum_i \frac{\langle u_i|R\rangle}{\omega_i^2 - \omega^2}|u_i\rangle. \tag{4.54}$$

The relevant eigenmodes are ω_2, ω_3, ω_4 and ω_5, (ω_1 is just translation motion of the structure). Now we can write the induced dipole moment, for each atom,

$$\begin{cases} p_1 = q_1\left(z_1 - z_1^{(0)}\right) = \frac{q}{\sqrt{m}}u_1 \\ p_2 = q_2\left(z_2 - z_2^{(0)}\right) = \frac{-q}{\sqrt{M}}u_2 \end{cases}. \tag{4.55}$$

We can define a polarisation vector,

$$|P\rangle = \begin{bmatrix} p_1 \\ p_2 \end{bmatrix} = \hat{Q}|u_f\rangle \tag{4.56}$$

And then the additional energy of the an uniform electric field is

$$\mathcal{E} = -\int_0^{|E\rangle} \langle P|\mathrm{d}E\rangle \tag{4.57}$$

with $|E\rangle \equiv E(1,1)$ as the electric field is uniform. The additional energy is written as [18]:

$$\mathcal{E} = -\frac{1}{2}\alpha E^2. \tag{4.58}$$

Therefore, the polarisability is,

$$\alpha = \frac{1}{E^2}\sum_{i=2}^{5} \frac{\langle u_i|R\rangle\langle E|\hat{Q}|u_i\rangle}{\omega_i^2 - \omega^2} = \frac{1}{E^2}\sum_{i=2}^{5} \frac{|\langle u_i|R\rangle|^2}{\omega_i^2 - \omega^2}. \tag{4.59}$$

It is convenient to introduce the oscillator strength, which determines the contribution of the vibration modes to the polarisability.

$$f = \frac{|\langle u_i|R\rangle|^2}{E^2} = \frac{q^2\left(\frac{1}{\sqrt{m}} - \frac{\beta}{\sqrt{M}}\right)^2}{(1+\beta)^2} \tag{4.60}$$

which leads to

$$\alpha = \frac{f}{\omega_A^2 - \omega^2} + \frac{2f}{\omega_S^3 - \omega^2}. \tag{4.61}$$

In reality the oscillations are always damped due to different natural reasons. This is taken into account by introducing a damping parameter Γ:

$$\alpha = \frac{f}{\omega_S^2 - \omega^2 - i\Gamma\omega} + \frac{2f}{\omega_A^2 - \omega^2 - i\Gamma\omega}. \tag{4.62}$$

So, the polarisability is a complex quantity with the imaginary part given by:

$$\mathrm{Im}(\alpha) = \frac{\Gamma\omega^2 f}{\left(\omega_S^2 - \omega^2\right)^2 - \Gamma^2\omega^2} + \frac{\Gamma\omega^2 2f}{\left(\omega_A^2 - \omega^2\right)^2 - \Gamma^2\omega^2} \tag{4.63}$$

where the oscillator strength is:

$$f = q^2 \frac{\left(\frac{1}{\sqrt{m}} - \frac{\beta}{\sqrt{M}}\right)^2}{(1+\beta^2)} \simeq \frac{q^2}{\mu}. \tag{4.64}$$

4.3 Stretching vibrations of a C-H bond on top of graphite basal plane

In this section we will study the vibration of a hydrogen atom adsorbed on the top of a graphite/graphene surface visually called "basal plane". Several recent studies indicates that such atom creates a covalent link with as the underlying carbon atom, which will result in a transformation from C-sp^2 to C-sp^3 bonds [36, 19, 22]. As a result, the C equilibrium position changes (as illustrated in Figure 4.2), forming a cluster, which is similar to the one considered in Section 4.2. However in this situation the angle between the C-H bond and the C-C bonds is not necessarily equal to the tetrahedric one ($\theta \neq \theta_0$) as it was in the Section 4.2 (see Figure 4.2).

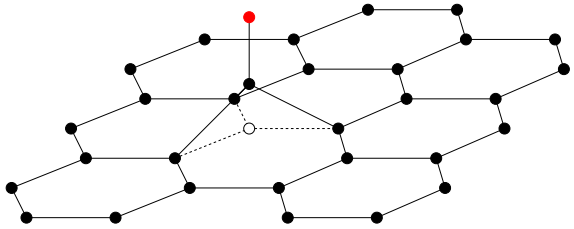

Figure 4.2: Sheet of graphene with one hydrogen atom on top of the surface, linked to one carbon atom.

For this situations it is possible to apply directly the results obtained in the previous section, making the following replacement:

$$\gamma \to \gamma' = \cos^2(\theta). \tag{4.65}$$

We shall assume that $\gamma' < \gamma$, i.e.

$$\frac{\pi}{2} < \theta < \arccos\left(-\frac{1}{3}\right). \tag{4.66}$$

In other words, $\gamma' < \gamma$ means that the elevation of the carbon atom is smaller than it would be for the true tetrahedric bonding. This is supported by DFT calculations: according to [19], the bond angle is $\theta \simeq 104°$ for the CCH bond 114° CCC for bond $\simeq 114°$ for the nearest neighbours.

The characteristic frequencies of the dipole-active modes, ω'_A and ω'_S are separated by:

$$\omega'^2_S - \omega'^2_A = 3\gamma'^2 \frac{k^2\mu^2}{k'M^3}. \tag{4.67}$$

As compared to $\omega_0^2 = \frac{k'}{\mu}$, the separation is smaller by a factor of

$$3\gamma'^2 \frac{k^2\mu^3}{k'^2M^3}. \tag{4.68}$$

Since $\mu \simeq \frac{M}{6}$ and $\gamma' \approx \frac{1}{10}$, the separation should be more than 10^3 times smaller than ω'^2_S and ω'^2_A and is given by:

$$\omega'_S - \omega'_A \simeq \frac{\omega'^2_S - \omega'^2_A}{2\omega'_0}. \tag{4.69}$$

This means that it should be hard to resolve theses modes experimentally. Thus, we conclude that such sp^3-bonded C-H clusters may be responsible for only one feature in the IR spectra.

4.4 Bond stretching vibrations of a cluster with two H atoms attached to a graphene sheet

Let us now consider an 8 atoms cluster containing two hydrogen atoms attached to two neighbouring C atoms (see Figure 4.3). We shall consider this configuration because chemisorption of hydrogen is possible on both sides of a graphene sheet [23]. The bond length connecting atoms 2 and 5 (See Figure 4.3b) is longer than the others. However, atoms 2 and 5 will have the same charge, transferred by the hydrogen atoms, so we shall model the bond 2-5 with a different stiffness (k'').

The symmetry of this cluster is C_{2h}. There is a 2-axis perpendicular to the sheet, passing through the middle of the 2-5 bond. The basal plane of the graphene sheet (where are located atoms 1, 2, 5 and 8) is a symmetry plane, perpendicular to the rotation axis. Irreducible representations of the group are called the A_g, A_u, B_g and B_u, all one-dimensional (it means symmetric with respect to inversion in the central point, u is antisymmetric).

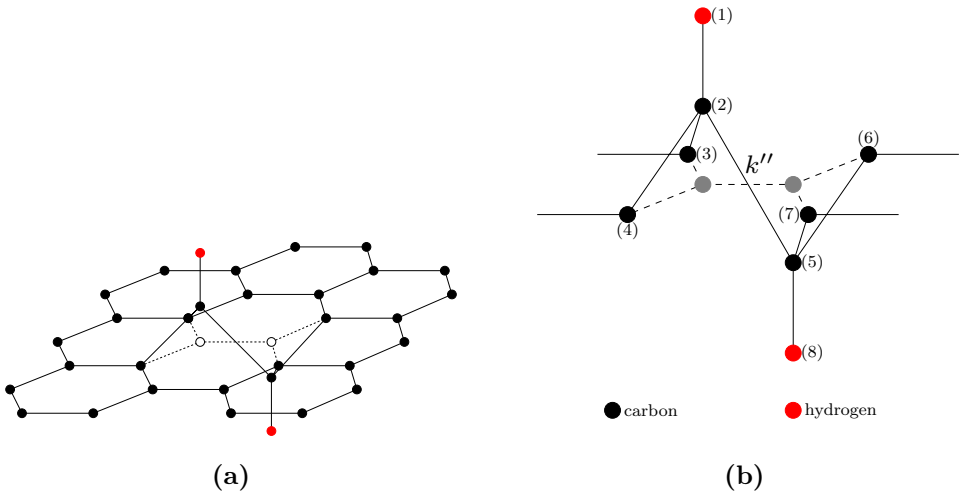

Figure 4.3: (a) Graphene sheet with two hydrogen atoms attached to the top and the bottom of the basal plane; (b) a more detailed diagram of the C-H bonds in the center of the sheet showing the atomic cluster considered explicitly.

Symmetric vibrations with $u_5 = -u_2$ are not dipole active because the dipole moments of the two C-H bonds cancel each other. Therefore, we are interested only in antisymmetric modes with $u_5 = u_2$ (so that a rotation by π around the symmetry axis (shown in the figure), changes the direction of atom's motion).

Furthermore, these modes, can be: (i) even (representation B_u, $u_3 = u_4 = u_5 = u_7$), or (ii) odd (representation B_g, $u_3 = -u_4 = -u_5 = u_7$), with respect to reflection in the vertical plane.

(i) B_u modes

The reduced dynamical matrix is:

$$\hat{D} = \begin{bmatrix} \frac{k'}{m} & -\frac{k'}{\sqrt{mM}} & 0 \\ -\frac{k'}{\sqrt{mM}} & \frac{k'+2\gamma' k}{M} & -\frac{2\gamma' k}{M} \\ 0 & -\frac{2\gamma' k}{M} & \frac{2\gamma' k}{M} \end{bmatrix}. \tag{4.70}$$

The last line in (4.70) represents the motion of the atoms 3 and 4, $u_3 = u_4 = u$, so the kinetic energy must be taken as $-2\omega^2 u$.

The high frequency mode is given by:

$$\begin{aligned} \omega^2_{B_u} &= \frac{1}{2}\left[\left(\frac{k'}{\mu} + \frac{3\gamma k}{M}\right) + \sqrt{\left(\frac{k'}{\mu} - \frac{3\gamma k}{M}\right)^2 + \frac{8\gamma k' k}{M^2}}\right] \\ &\simeq \frac{k'}{\mu} + \frac{2\gamma k \mu}{M^2} + 6\frac{\gamma^2 k^2 \mu^2}{k' M^2} \end{aligned} \tag{4.71}$$

(ii)B_g mode

For this mode the reduced dynamical matrix is:

$$\hat{D} = \begin{bmatrix} \frac{k'}{m} & -\frac{k'}{\sqrt{mM}} \\ -\frac{k'}{\sqrt{mM}} & \frac{k'-2\gamma k}{M} \end{bmatrix}, \tag{4.72}$$

giving for the frequency of the high-frequency mode:

$$\begin{aligned} \omega_{B_g}^2 &= \frac{1}{2}\left[\left(\frac{k'}{\mu}+\frac{2\gamma k}{M}\right)+\sqrt{\left(\frac{k'}{\mu}-\frac{2\gamma k}{M}\right)^2+4\left(\frac{12\gamma k k'}{M^2}\right)}\right] \\ &\simeq \frac{k'}{\mu}+\frac{2\gamma k\mu}{M^2}+4\frac{\gamma^2k^2\mu^2}{k'M^2}. \end{aligned} \tag{4.73}$$

We conclude that the frequency of the modes ω_{B_u} and ω_{B_g} are slightly shifted with respect to $\omega'_A \simeq \omega'_S$ [compare to equation (4.35) or (4.40)] meaning that from the experimental point of view they hardly can be separated in experiments. The shift (to lower frequencies) with respect to the modes of the one hydrogen atom cluster is:

$$\Delta\omega \simeq \frac{\omega_{B_g}^2-\omega_A'^2}{2\omega'_A} \simeq \frac{\frac{\gamma' k\mu}{M^2}}{\sqrt{\frac{k'}{\mu}}} \tag{4.74}$$

or

$$\frac{\Delta\omega}{\omega_0} \simeq \gamma\frac{k}{k'}\left(\frac{\mu}{M}\right)^2. \tag{4.75}$$

It means that for $\gamma \approx \frac{1}{10}$, $k \approx k'$ and $\left(\frac{\mu}{M}\right)^2 \approx \frac{1}{6}$, we have $\Delta\omega \simeq 7-8$ cm^{-1}.

Therefore these types of clusters that contain hydrogen atoms sitting slightly above (or below) a graphene sheet probably cannot explain the rather broad variety of vibrational modes observed in the range from 2850 to 2955 cm^{-1}.

4.5 Bond stretching vibrations of a C-H on the edge of graphene sheet

We will now study the vibration properties of a hydrogen atom bonded to a carbon atom of the edge of a graphene crystal. The graphene honeycomb lattice can be cut along two primary directions, $(1\bar{1}0)$ and $(2\bar{1}0)$, creating so-called armchair and zigzag/Klein edges respectively (see Figure 4.4) [37]. Armchair edges are stable with respect to reconstruction, also when terminates with two hydrogen atoms at each carbon atom (see Figure 4.5a). The zigzag edges are much less stable, either single or double hydrogenated (see Figure 4.5b). Instead, hydrogenated Klein edges containing CH_3 groups (see Figure

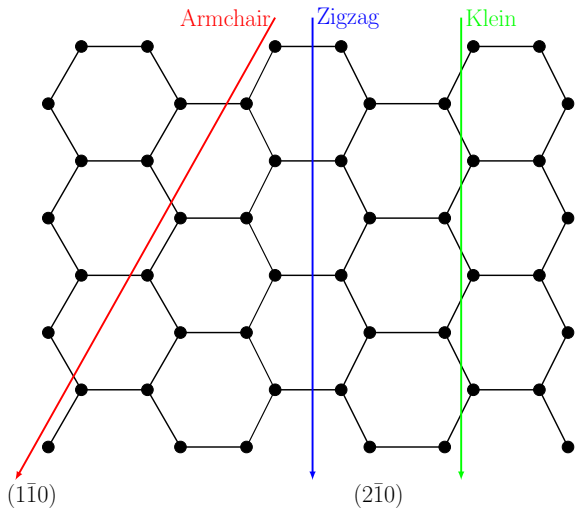

Figure 4.4: Scheme of three types of the edges of grafene: Armchair edge (red), Zigzag edge (blue) and Klein edge (green) [37].

4.5c) approaches in stability to the hydrogenated armchair edges [37]. These edge groups can undergo significant out of the plane edge rippling.

Simple H atoms attached to armchair or zigzag edges can occur even if such configurations are less stable a those involving more than one hydrogen atom; they can be be statistically more frequent under limited supply of hydrogen.

However, it is known that the frequencies of the sp^2 =C-H modes appear at frequencies higher than 2975 cm^{-1} [1], meaning that do not correspond to the observed experimentally in our samples. Therefore, we will consider clusters formed at the graphene edges but with more than one hydrogen atom (i.e. 2 or 3 atoms), as shown in Figure 4.5a and 4.5c, with chemical bonds of the essential carbon atom transformed into the sp^3 type.

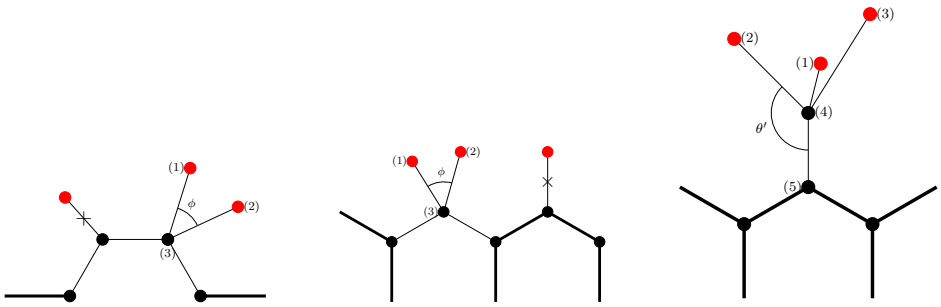

(a) **(b)** **(c)**

Figure 4.5: Scheme of edge of a graphene sheet with (a,b) two and (c) three hydrogen atoms attached to it (sp^2-type bonds are shown thicker). The configuration (a)-(c) correspond to the armchair, zigzag and Klein edges, respectively.

In the cluster presented in Figure 4.5a, the two hydrogen atoms do not lie in the plane of the graphene sheet and the angle between the bonds 1-3 and 2-3 is denoted by ϕ. Based on the previous study we will consider explicitly only one carbon atom (#3 and #4 for Figure 4.5b and 4.5c, respectively) because the motion of the other carbon atoms only introduce small-scale changes in the C-H vibration frequency. So, we will consider their displacements as equal to zero.

However, the main difficulty in study these kind of clusters, is related to the fact that the hydrogen atoms are charged and, therefore interact with each other and this interaction cannot be modelled by adding an effective spring. Indeed the Coulomb repulsion is direct but the attractive part, that stabilizes the system, occurs indirectly, involving other carbon atoms and it defines the value of the angle ϕ between the C-H bonds. We can demonstrate the impossibility of modelling the H-H interaction with an effective spring by performing the following simple calculation. Let us make a rude but still reasonable approximation that the attached carbon atom (#3 in Figure 4.5a) does not move at all. Then the system of two masses and three springs possesses two vibrational modes (point O is fixed, see Figure 4.6).

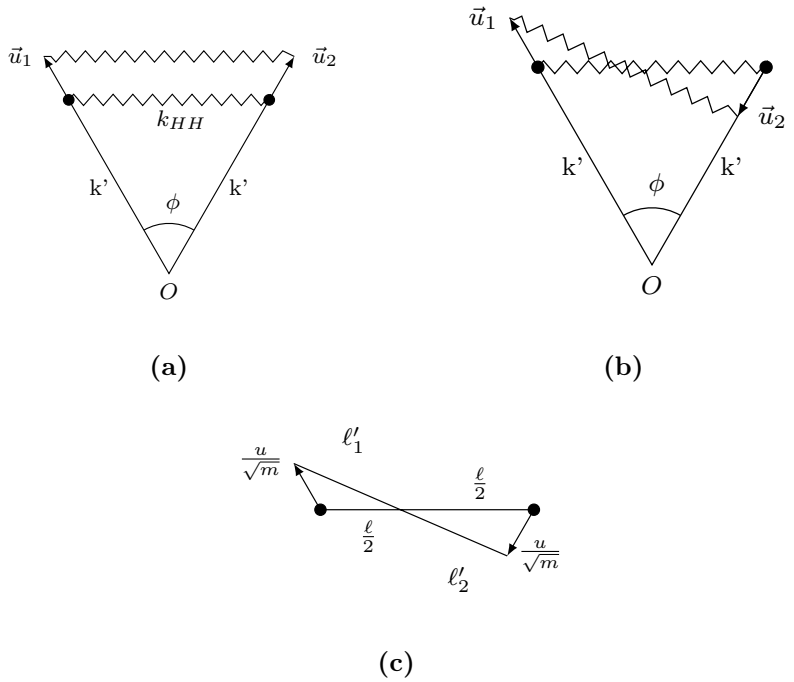

Figure 4.6: The illustration of the atomic displacements in a cluster containing two hydrogen atoms and one fixed carbon atom, for (a) symmetric and (b) antisymmetric mode; (c) is an auxiliary picture for the calculation of the elongation of the H-H spring.

The elongation of the effective spring in the symmetric case (of Figure 4.6a) is:

$$\triangle\, \ell_{12} = \frac{1}{\sqrt{m}}|\vec{u}_1 - \vec{u}_2| = \frac{2u}{\sqrt{m}} \sin\left(\frac{\phi}{2}\right). \tag{4.76}$$

If we denote the effective stiffness of the H-H spring by k_{HH}, the Lagrangian of the system becomes:

$$\mathcal{L} = \frac{1}{2}\left(2\dot{u}^2\right) - \frac{2k'}{2}\left(\frac{u}{\sqrt{m}}\right)^2 - \frac{k_{HH}}{2}\left(\frac{2u}{\sqrt{m}}\sin\left(\frac{\phi}{2}\right)\right)^2 \tag{4.77}$$

and the vibration frequency is

$$\omega_{2S} = \sqrt{\frac{1}{m}\left(k' + 2k_{HH}\sin^2\left(\frac{\phi}{2}\right)\right)}. \tag{4.78}$$

For the situation of Figure 4.6b, we find for the spring length (see Figure 4.6c):

$$\begin{aligned} \ell'_{12} &= \ell'_1 + \ell'_2 \\ &= \sqrt{\left(\frac{\ell_{12}}{2}\right)^2 + \frac{u^2}{m} - 2\frac{u}{\sqrt{m}}\left(\frac{\ell_{12}}{2}\right)\cos\left(\frac{\pi \pm \phi}{2}\right)} \end{aligned} \tag{4.79}$$

(where we applied the cosine theorem).

Therefore, to the first order in u, we have:

$$\ell'_{12} \simeq \frac{\ell_{12}}{2} + \frac{u}{\sqrt{m}}\sin\left(\frac{\phi}{2}\right) + \frac{\ell_{12}}{2} - \frac{u}{\sqrt{m}}\sin\left(\frac{\phi}{2}\right) = \ell_{12} \tag{4.80}$$

and

$$\omega_{2A} = \sqrt{\frac{k'}{m}} < \omega_{2S}. \tag{4.81}$$

However, it is known that for a 3-atomic molecules system, the asymmetric mode has a higher frequency than the symmetric one [18] and then we conclude that the effective spring model fails to reproduce it.

Therefore, we shall follow the consensual interpretation found in the literature: the symmetric and antisymmetric vibration of the sp^3-CH_2 cluster, related to stretching of the C-H bonds correspond to the frequencies [20, 21]:

- $\omega_{2S} = 2850\ \text{cm}^{-1}$;
- $\omega_{2A} = 2920\ \text{cm}^{-1}$;

i.e. $\omega_{2A} > \omega_{2S}$.

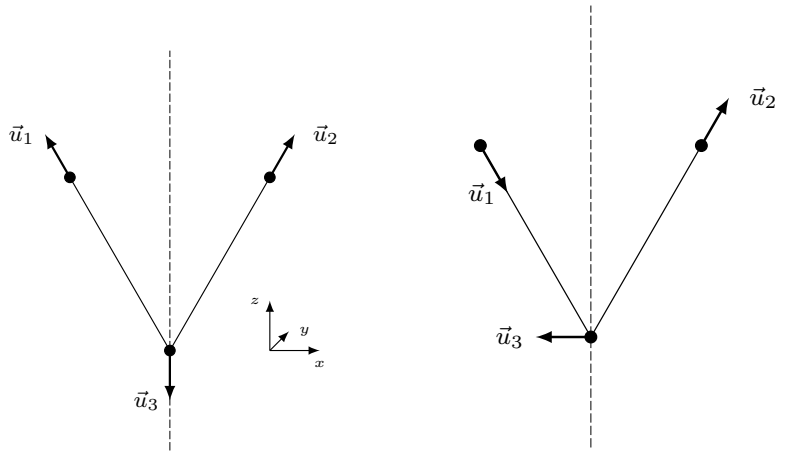

(a) **(b)**

Figure 4.7: Representation of (a) symmeric A_1 mode and (b) asymmetric and B_1 mode of a 3-atom cluster.

The symmetry group of the cluster CH_2 is C_{2v} (one 2-axis and two vertical symmetric planes). The symmetric and asymmetric modes belong to irreducible representations A_1 and B_1, respectively, both one-dimensional (non-degenerate) [18].

The dipole moment due to these vibrations is:

$$\vec{p}_{2S} = 2q\frac{u}{\sqrt{\mu}}\cos\left(\frac{\phi}{2}\right)\vec{e}_z; \tag{4.82}$$

$$\vec{p}_{2A} = 2q\frac{u}{\sqrt{\mu}}\sin\left(\frac{\phi}{2}\right)\vec{e}_x. \tag{4.83}$$

Therefore, the oscillation strengths of these modes are related by:

$$\frac{f_{2A}}{f_{2S}} = \tan^2\left(\frac{\phi}{2}\right). \tag{4.84}$$

If $\phi > \frac{\pi}{2}$, $f_{2A} > f_{2S}$ as it happens for the modes observed in the literature [20, 21], with the assignment given above. In particular, for $\phi = 2\arctan\sqrt{2} \simeq 109°$, $\frac{f_{2A}}{f_{2S}} \simeq 2$ as observed in experiments [20, 21].

The analysis of vibrational modes of the sp^3-CH_3 clusters is similar to the one performed in the beginning of this chapter for a fragment of the diamond lattice with one hydrogen atom replacing a carbon atom. Here the atoms are exchanged, C$\rightleftarrows$H, and the angle between the adjacent bonds is $\theta' \neq \theta_0$. Yet the symmetry is the same (C_{3v}), with one non-degenerate [18] (A_1) and a couple of double-degenerate (E) asymmetric modes. According to the literature for C-H compounds [1] and also for Si-H materials [24], we assume that $\omega_{3A} > \omega_{3S}$.

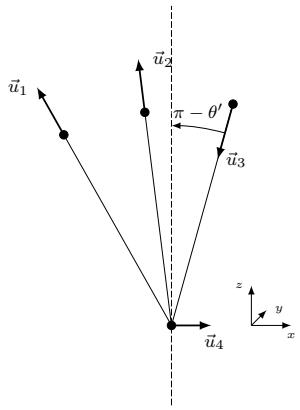

Figure 4.8: A 4-atom cluster with 3 hydrogen atoms formed at a Klein edge. The arrows show atomic displacement corresponding to asymmetric (E) modes.

Similar to equations (4.82) and (4.83), we have

$$\vec{p}_{3S} = 3q\frac{u}{\sqrt{\mu}}\cos(\pi - \theta')\vec{e}_z; \tag{4.85}$$

$$\vec{p}_{3A} = -3q\frac{u}{\sqrt{\mu}}\sin(\pi - \theta')\vec{e}_x. \tag{4.86}$$

The oscillator strengths of these modes are related by:

$$\frac{f_{3A}}{f_{3S}} = 2\tan^2(\pi - \theta'), \tag{4.87}$$

where the factor 2 represents the degeneracy of the asymmetric mode. We tentatively associate these modes with the experimentally observed features, with the frequencies:

- $\omega_{3S} \simeq 2870\text{cm}^{-1}$;
- $\omega_{3A} \simeq 2955\text{cm}^{-1}$.

This assignment is based in the (approximate) correlation of these modes intensity in our experimental spectra as discussed in the Chapter 6.

4.6 IR mode assignment

Based on the theoretical considerations presented above we can now make the assignments of the modes measured experimentally. Figure 4.9 shows an "IR absorbance" $[1 - R_{ATR}(\omega)]$ obtained from the ATR spectra of one of our samples, fitted in the 2600-3200 cm^{-1} frequency range.

This spectrum can be fitted fairly well with five Lorentzians as shown in the Figure 4.9. The details of the modelling procedure are left for Chapter 5 and Appendix. The

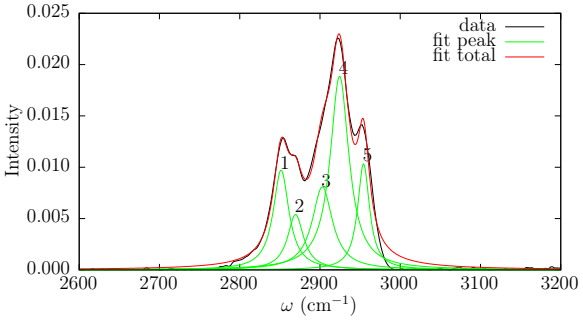

Figure 4.9: ATR reflectance subtracted from unity, $[1 - R_{ATR}(\omega)]$ C-H modes with baseline at zero intensity, fitted with five Lorentzian fit, of samples 3.

diagram shown in Figure 4.10 corresponds to our assignments based mostly on the considerations presented above in this Chapter. The numbers are mode frequencies for samples #3. We have some doubts concerning the peak 3 assignment, which in fact

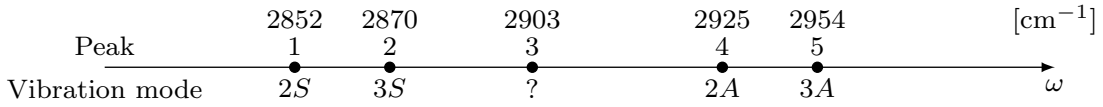

Figure 4.10: Diagram showing the assignment of the C-H modes.

appears as a shoulder in the experimental spectrum. This peak may correspond to the mode due to the H atom sitting on the top of a graphene sheet. Indeed from our model we expect several modes at frequencies very close to each other.

However, DFT calculation results do not corroborate this possible assignment [19], according to then, basal chemisorption produces modes at 2800 and 2871 cm^{-1}. Yet, according to these calculations the modes at $\simeq$ 2850 and 2920 cm^{-1} indeed come from hydrogenated Klein edges.

For the sake of completeness, many other IR-active modes come out of these calculations, for hydrogenated graphene edges, in particular, in the frequency range below 1000 cm^{-1} [38]. We do not analyse these modes since they are not clearly observed in our experimental spectra.

5. Modelling of FTIR and ATR spectra

5.1 Theoretical models of reflectance for multilayer samples

Our aim here is to model the experimental reflectance spectra. It requires multilayer optics treatment to take into account multiple reflections at each surface or interface and the resulting interference effects. We shall use the transfer matrix formalism [30], which is presented in detail in Appendix A and yields the Fresnel coefficients, $\hat{r}_p$ and $\hat{t}_p$ (we shall consider the case of p-polarized light).

The reflectance of the whole structure is:

$$R(\omega) = |\hat{r}_p(\omega)|^2 \tag{5.1}$$

and the wavevectors to be used in equation (A.26) are:

$$k_x = \sqrt{\varepsilon_1}\frac{\omega}{c}\sin(\theta); \tag{5.2}$$

$$k_{zj} = \sqrt{\varepsilon(\omega)_j\left(\frac{\omega}{c}\right) - k_x^2}, \tag{5.3}$$

where $\theta = 0$ for normal incidence of the light and $j = 1, 2, ...$ correspond to the different layers of the structure including substrate.

Table 5.1: Parameters of the dielectric function for C:H, SiO_2 and Si [39, 40, 41, 42] and frequencies of C-H vibration modes from the experimental data for sample #3.

	$\varepsilon(\omega)$				C-H modes frequencies and damping			
	$\omega_p(\text{cm}^{-1})$	$\Gamma(\text{cm}^{-1})$		ε_∞	Bonds	ω_i (cm^{-1})	Γ_i (cm^{-1})	
Graphite	3548.3	166.8		3	CH	2903.10	29.71	
Transition Metal	48400	433		1	CH_2	2850.32	24.72	Symmetric
	ω_{LO}	ω_{TO}	Γ	ε_∞	CH_3	2869.20	28.79	Symmetric
SiO_2	1243.5	1065.5	61.6	1.843	CH_2	2923.95	27.81	Asymmetric
Si				11.696	CH_3	2953.79	16.79	Asymmetric

Table 5.1 present the parameters used in the modelling.

The dielectric function of the carbon film, $\varepsilon_2(\omega)$ is composed of two parts, the Drude model term and the term representing the contribution of polar vibrations:

$$\varepsilon_2(\omega) = \varepsilon_\infty - \frac{\omega_p^2}{\omega^2 + i\Gamma_p\omega} + \sum_n \frac{f_n}{\omega_n^2 - \omega^2 - i\Gamma_n\omega} \tag{5.4}$$

Here ω_p and Γ_p are the plasma frequency and damping. The frequencies and oscillator strengths are those discuses in the Chapter 4.

We studied by calculating the spectra using normal incidence of a free standing hydrogenated carbon layer, changing the layer thickness between 300nm and 1000nm. The results are shown in Figure 5.1. The spectra are characterized by a minimum at aprox 2500 cm^{-1} (independent of the layer thickness) which corresponds to the plasma frequency of the graphite. Between 2800 cm^{-1} and 3000 cm^{-1} several features are seen, which are related to vibration of the carbon-hydrogen bonds. Indeed the intensity of these peaks increases as the layer thickness grows. For higher wavenumbers it is seen the appearance of interference fringes, as the layer thickness increases.

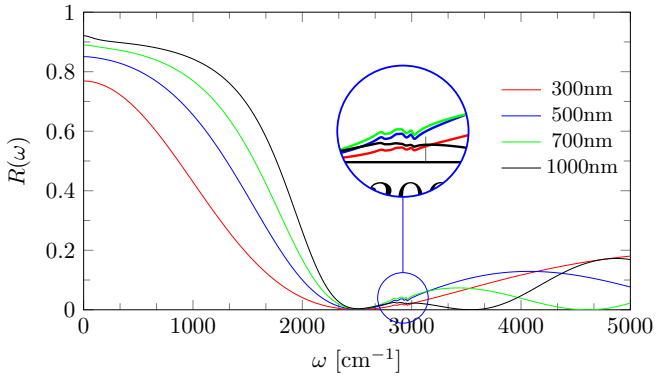

Figure 5.1: Reflectance of free standing C:H films with different thickness.

Now we shall include the substrate in our simulations. Unfortunately, the precise composition of the steel substrates used to grow our samples is not known. The reflectance spectra of steel are complex [35] and can not be described by a Drude-type model suitable for alkaline or noble metals. Investigation of the dielectric function of steel was out of scope of the present study. Therefore we tried some simple models for describing the substrate, which is a rather imperfect reflector.

The Calculated reflectance spectra of the film placed on a Drude metal is shown in Figure 5.2a. This substrate acts as a nearly perfect mirror in the IR range. The characteristic absorption modes related to the C-H vibrations are clearly seen in the calculated spectra, and it is seen that their intensity increases with the increase of the carbon layer thickness.

As an example of the imperfect mirror, we consider a Si/SiO_2 substrate (100nm of silicon oxide on top of 100μm thick silicon slab); such substrates are often used for

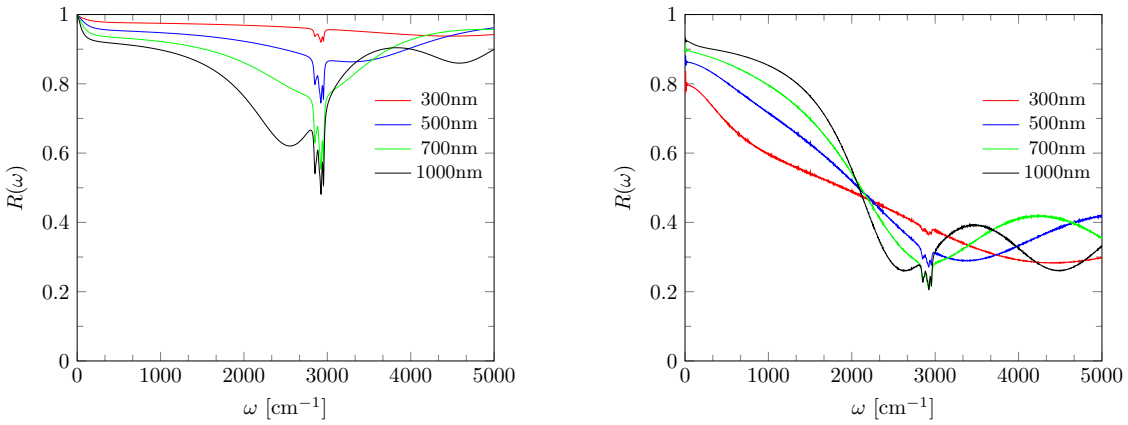

(a) **(b)**

Figure 5.2: Calculated reflectance spectra for different thickness of C:H layer in two types of samples: (a) on a 100μm Drude metal slab, (b) SiO_2/Silicon substrate.

research purposes. The calculated results are shown in Figure 5.2b. It is seen the effect of a non-perfect metallic substrate, by the decrease of the reflectance in the whole frequency range. Furthermore, the C-H modes become less intense, mainly due to the presence of interference fringes because of the light reflection on the back surface of the substrate (which would hinder the C:H modes in the spectra). However, the general trend of the intensity increase of these modes with the increase of the carbon layer thickness is still seen. To overcome the interference fringes effect, we averaged these spectra, over a Gaussian distribution of slab thickness with a standard deviation of 20 μm. As a result, the refection reduces by about 50% , in the frequency range of the C-H modes, but the hydrogen-related features become more evident and clearly seen in the spectrum, at least for the carbon layer thickness of 1000nm. These calculations were performed for illustrating the substrate effect on the calculated reflectance spectra. In this way we demonstrate that the unknown substrate used of our samples, that make the experimental reflection spectra "imperfect" is not a limitation for the observation and analysis of the hydrogen-related features.

5.2 Attenuated Total internal Reflection (ATR) spectra

In this section, we calculated the ATR spectra of the C:H layers structures. As discussed in Section 2.2.2, this method is used for detection of the surface waves such as surface plasmon-polaritons, which is not the purpose of the present work. However, using the ATR configuration, for our study, revealed that this configuration allows a better C-H signal (when compared to R-FITR) and in this way permits a better characterisation of the material under study. Since the sample interacts with an electromagnetic wave

whose amplitude decreases exponentially inside the sample, only the near-surface region of the sample is probed, which means that the unknown substrate will not influence the result, resulting that the C-H modes will be more clearly seen.

For the ATR spectra calculation, the same transfer matrix formalism described before was used, but including the prim. The prism was modelled as a half-space with dielectric constant ϵ_p. The incident angle was $\theta > \theta_0$. For this study we also considered two types of structures: (i) free-standing C:H layer and (ii) C-H layer deposited on a Drude metal slab.

For the first case, free-standing C:H layer (250nm thick), the calculations were performed for two configurations: the Otto and Kretschmann ones. The obtained results are shown in Figure 5.3.

The prominent feacture, seen in both spectra, at $\simeq$2000 cm^{-1} correspond to the surface plasmon-polariton mode. Although shifted, it is related with the plasma frequency of graphite (3000 cm^{-1} corresponding to 0.44 Ve [39]). The calculated spectra also show small features related with C-H vibrations in the range around 2900 cm^{-1}, although more clear seen for the Kretschmann configuration (with no gap between the sample and the prism).

In the Otto configuration, we see also a gap mode appearing at $\simeq$1000 cm^{-1}. In fact, it is also a surface plasmon-polariton, however centered at the air/graphite interface, which is located closer to the prism, as shown below.

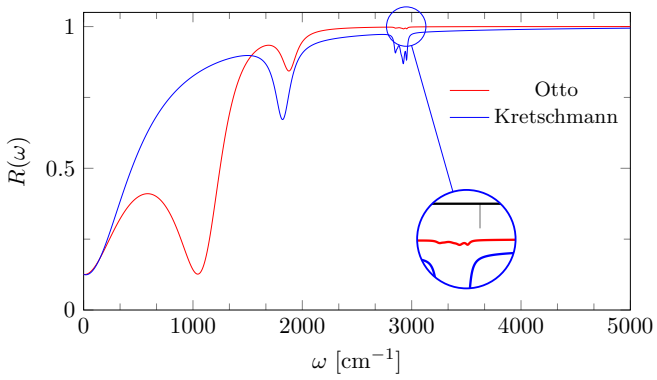

Figure 5.3: Calculated ATR spectra for 250nm free-standing C:H layer in Otto configuration with the gap 250nm and in the Kretschamann configuration.

In the Otto configuration (Figure 2.4a) with air gap and a free standing C:H film, there two air/graphite interfaces, both supporting surface waves. They are not equivalent with respect to the prism and therefore produce two distinct features in the ATR spectrum [1].

[1] As known, the position of the reflectivity dip depends on the distance between the plasmonic interface and the prism [30].

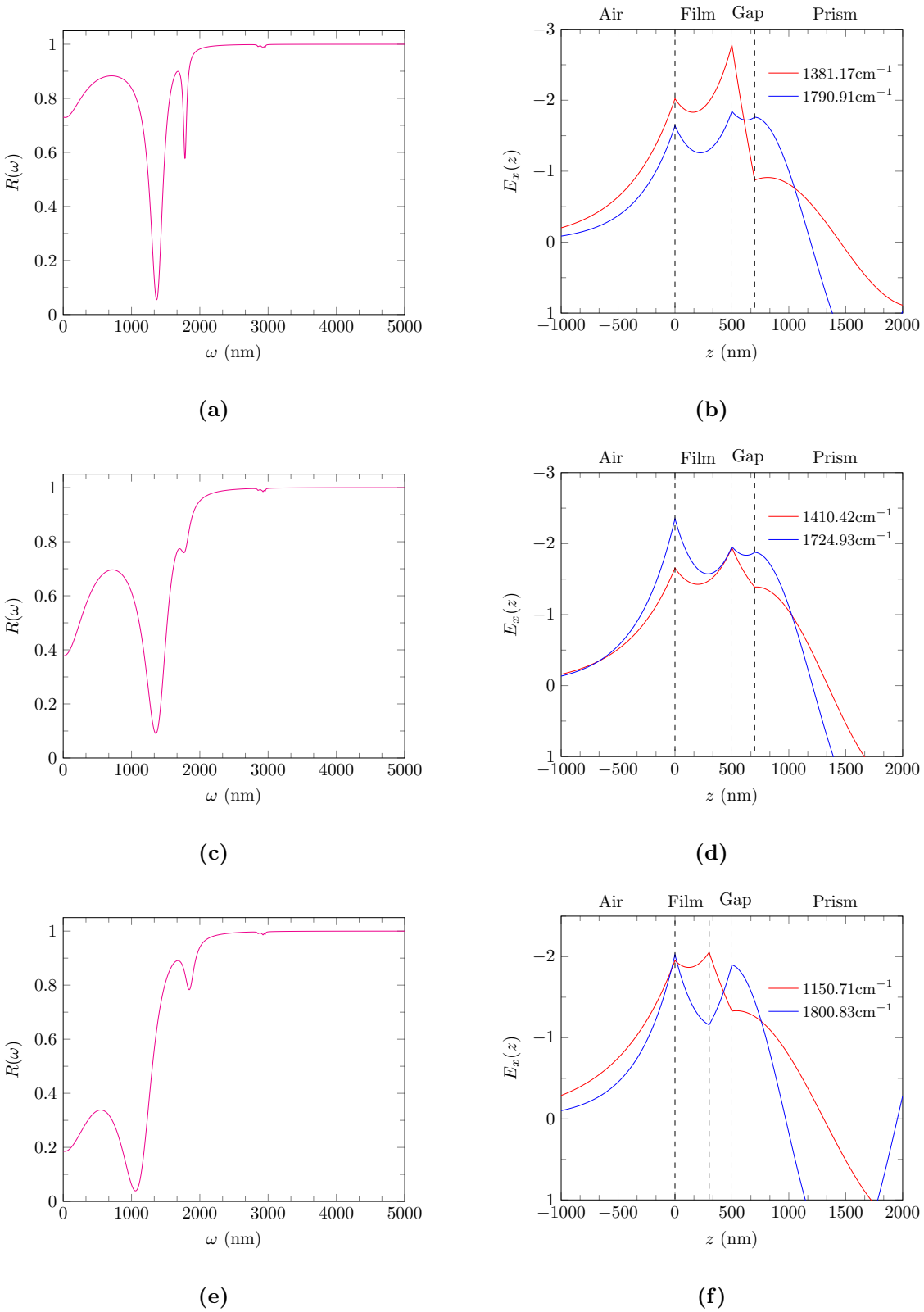

Figure 5.4: Calculated ATR spectra and corresponding profiles of transverse electric field across the structure for suspended C:H film in Otto configuration with 200 nm gap (a, b) d=500nm, reduced plasmon damping Γ_p =0.0068 eV (c, d) d=500nm, Γ_p =0.02068 eV (e, f) d=300nm, Γ_p = 0.02068 eV.

We exemplify it in Figure 5.4 where the left panels show the spectra for two different widths of the air gap (500 nm in 5.4a and 5.4c and 300 nm in 5.4e) and the right ones present the corresponding profiles of the transverse electric field component for two characteristic frequencies in each case (the origin of z axis is chosen at the back side of the carbon layer).

In Figures 5.4a and 5.4b the graphite plasmon damping was artificially reduced to 0.00068 eV, which allows us to see the spectral features more clearly and calculate the field profiles exactly for these situations. According to Figure 5.4a, the spectral feature at 1381.17 cm^{-1} corresponds to the surface wave travelling along the carbon/gap interface, while the other one (1790.91 cm-1) is less intense in the spectrum because it occurs at the back surface, more remote from the excitation prism.

In Figure 5.4c plotted for a more realistic value of plasmon damping (0.02068eV), this second feature is rather weak and can easily be overlooked in real experiments. Yet, the field profile of Figure 5.4d clearly shows that this surface wave still is excited.

It is interesting to see that the surface modes located at the opposite sides of the film begin to interact when the film thickness becomes smaller (Figures 5.4e and 5.4f). Indeed, we notice that the two spectral features "repulse" (notice the mode frequencies in the plot) and the field profiles also change. For the low frequency mode (red curve in Figure 5.4f), the field amplitude is approximately the same at both interfaces. Such a mode can be called acoustic as the electric fields at two interfaces are in phase, like vibrations of two atoms in the same unit cell in an acoustic phonon mode. In contrast, the other mode (blue curve in Figure 5.4f) corresponds to clearly distinct field amplitudes at two sides of the film; such a mode may be called "optical".

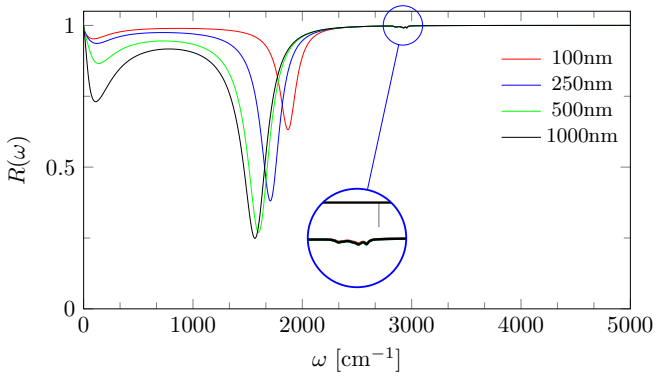

Figure 5.5: Calculated ATR spectra for different thickness of the C:H layer with a Drude metal as substrate.

Figure 5.5 presents ATR spectra calculated, for the Otto configuration, for carbon/metal structure with different carbon layer thickness. The simulated spectra present one main band, that shifts to lower wavenumber and increases in intensity with the increase of the carbon layer thickness. The simulated spectra also show the feature related to C-H bonds, but with low intensity. Comparing the C-H features obtained in the Otto configuration without (red curve in Figure 5.3) and with substrate (red curve

in Figure 5.5), for the same carbon layer thickness, it is seen that the intensity is much lower for the system with substrate.

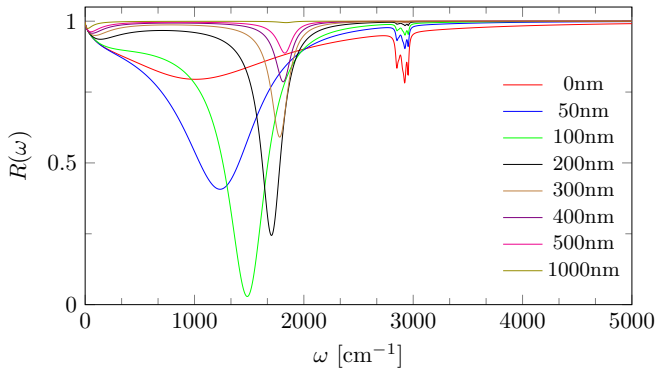

Figure 5.6: Calculated ATR spectra of a 200 nm thick C:H layer on a metal substrate for different air gap thicknesses as indicated on he plot (Otto configuration).

Figure 5.6 shows the spectra of a 200 nm thick graphite film on a Drude metal substrate, calculated for different gap widths (the case of zero gap corresponds to the Kretschman configuration). As can be seen from this figure, the intensity of the surface-plasmon-related features varies non-monotonically with the gap size. This is because the plasmon becomes strongly damped for small gaps (very broad ATR band), while the coupling to the exciting wave coming out of the prism becomes too weak for large distances. Thus, the gap size can be optimized if the objective is to study the surface wave. In what concerns the intensity of the signal related to the C:H modes, it decreases monotonically with the gap size, so the most favorable situation for their observation corresponds to the Kretschman configuration. Unfortunately, it is not always possible to realize this configuration in practice.

To conclude this chapter, our modelled spectra show that the characteristic C-H modes can be observed by both conventional and ATR IR spectroscopy bur the latter is preferable because of better resolution and smaller influence of the poorly known substrate.

6. Discussion of spectroscopy and modelling results

6.1 Raman spectroscopy

The Raman study performed in these samples reveal that the carbon films are composed of a mixture of sp^2- and the sp^3- bonded fragments and the relative weight of these phases depends on the amount of H added during the growth. This conclusion was taken based on the peak position of the G mode and on the intensity ratio between the D and the G mode, following the Robertson's review [1]. For the samples produced using low hydrogen flux (corresponding to hydrogen <0.08), D peak intensity is lower than the peak G whereas for the samples grown with high H flux (corresponding to hydrogen > 0.1)the D and G intensity are very similar. Taking into account that we are in the first stage according to Robertson's classification [1] (which is the transition from graphite to nano-graphite ("graphene")), it indicates that the carbon atoms in the layers form a kind of graphite/graphene clusters with small sizes and consequent with borders (that originate the D mode) and favours the bonding of the hydrogen to the edges of the cluster, forming C-H bonds (see Figure 4.5 in Chapter 4). These C-H bonds will affect the A_{1g} vibration mode of carbon responsible for D peak associated with the stretching of the rings. With increasing exposure to hydrogen it is expected an increase of the number of C-H bonds at the edges, allowing the carbon atom at the edge to realize 1, 2 or even 3 bonds with hydrogen atoms. As a result, the stretching vibrations of the rings is enhanced (increase of the D mode intensity). However, If the hydrogen amount (during the growth) is too high, it will amorphize the carbon network and no more clusters (rings) will exist, (means no D mode), which means that $I(D)/I(G)$ should decrease [43, 44]. The C-H bands are not evident in the Raman spectra between 2850-3000 cm^{-1}, probably due to the fact that they have a low intensity and are hidden by the photoluminescence background, which is believed to be caused by the C-H bonds [45]. This background can be approximated, in a limited range by a linear function of frequency as suggested in Ref. [17]. We applied this procedure in order to perform the fitting of the G and D modes as shown in Appendix B.1. The slope of the linear function turns out to correlate with the fraction of hydrogen added during samples growth. Some researchers [17] use this correlation to determine the hydrogen content and when applied to our samples it follows a comprehensive behaviour (see Figure 6.1).

With the exception of one point (related to sample 1), we find that there is an increase of the steepness of the PL background with the increase of the amount of hydrogen, showing a good linear regression.

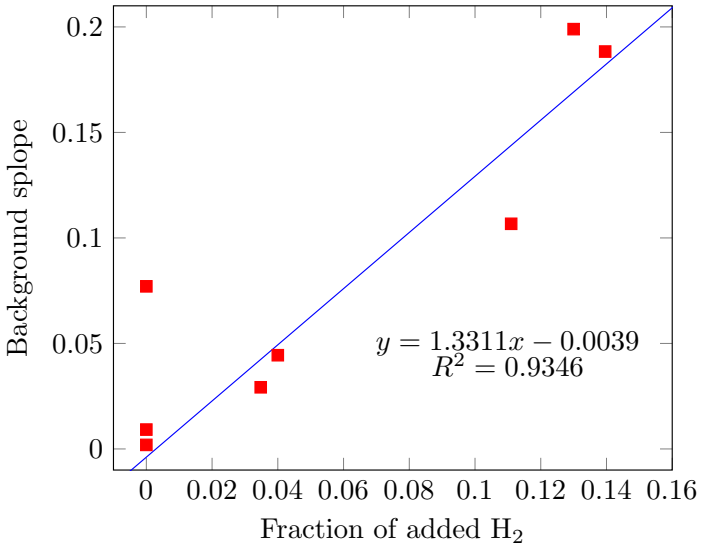

Figure 6.1: Fraction of hydrogen as a function of the slope of the line used to draw baseline to remove PL background in the Raman spectra.

This correlation, even though its mechanism is unclear to us at the moment, is quite evident.

However, the H content information is not in agreement with the results obtained by ERDA neither with the supplied information, neither with the Raman data.

6.2 IR spectroscopy

The IR spectroscopy results provide the most clear evidence of the presence of hydrogen forming (partially ionic) covalent bonds with sp^2-type bonded carbon atoms. The presence of hydrogen bonded to carbon atoms is seen by the presence of the characteristic absorption peaks in the range 2850-2900 cm^{-1} as well as by the observation of the plasma edge at frequencies around 2500 cm^{-1}. This plasma frequency is in agreement with the known plasma frequency of graphite ($\hbar\omega_p = 0.44$ eV [40], as shown by our model calculations for a free-standing film, Figure 5.1).

We have not been able to fit the R-FTIR spectra because of lack of information on the (presumably quite complex) IR dielectric function of the steel substrate. Assuming for the substrate the properties some what between a Drude metal and silica, we compared the spectra calculated for these two substrates beneath the carbon film, which are shown in Figure 5.2. Indeed it is possible to observe the C-H signatures.

ATR spectroscopy turns out to be a better option for studying the C-H bonds, since the spectra show better resolution of the absorption peaks related to C-H vibration modes. It is due to the fact that in ATR geometry the substrate almost does' not influence the spectra, as confirmed by the calculated results obtained with our model (Figure 5.5).

The ATR measurements were performed using the Otto configuration and the results shown in Figure 3.5 do show the expected signatures of the C-H bonds. For all samples, except # 1 and #8 (samples grown without hydrogen), the ATR spectra present the H-related features and also a band at $\simeq 1600$ cm^{-1} that was assigned to the surface plasmon-polaritons, from the graphite-like structure of the carbon films (discussed in Section 5.2). The ATR spectra are nearly "flat" in the range of C-H vibration modes, which allows for quantitative analysis (see Appendix B.2), which yields results that are summarized in Table 6.1. As can be seen in the Table 6.1, the positions of the peaks for each sample, except for samples #8 and #10, are identical (deviations <1 cm^{-1}). It is also seen that the area ratio between the fourth and the first peak is approximately equal to 2, which can indicate that these two peaks correspond to the symmetric and antisymmetric vibrations of the CH_2 cluster. Indeed, according to equation (4.84), these two peaks correspond to the angle between adjacent C-H bonds in the CH_2 "molecule" formed at an armchair edge of a graphene sheet, equal to $2\arctan\left(\sqrt{2}\right) \simeq 109.5°$. We notice that it is very close to the tetrahedric angle characteristic of sp^3 bonds.

Also, we notice that the intensity ratio of peak 5 and peak 2 varies between 1 and 1.5 for different samples but their intensities are considerably lower than those of the peaks 1 and 4. For this reason, we assign them to the CH_3 clusters shown in Figure 4.5c formed at Klein edges of graphene flakes. Such clusters contain 3 hydrogen atoms and therefore are statistically less probable than those of Figure 4.5a, containing only two H atoms. The intensity ratio for the 3H-clusters is given by equation (4.87), which implies that the angle between any two of adjacent C-H bonds in this case $\theta' \simeq (\pi - \arctan\left(\frac{1}{\sqrt{2}}\right)) \simeq 144.7°$ (taking $I_5/I_2 \simeq 1$).

The modes assigned to 2H and 3H clusters formed at the graphene/graphite crystal edges are presented in the diagram of Figure 4.10. Concerning the remaining peak 3, we notice that this peak is broader, where less in resolution and becoming difficult the assignment. We tentatively assign this band (possibly composed of more than one mode) to hydrogen atoms sitting on top of a graphene sheet (Figure 4.2 and also possibly Figure 4.3).

Table 6.1: The results of the fit we have the position, FWHM and area for each peaks.

run	Peak 1			Peak 2			Peak 3			Peak 4			Peak 5		
	ω	FWHM	area	ω	FWHM	area	ω	FWHM	area	ω	FWHM	area	ω	FWHM	area
	cm^{-1}	cm^{-1}	$(cm^{-1})^2$	cm^{-1}	cm^{-1}	$(cm^{-1})^2$	cm^{-1}	cm^{-1}	$(cm^{-1})^2$	cm^{-1}	cm^{-1}	$(cm^{-1})^2$	cm^{-1}	cm^{-1}	$(cm^{-1})^2$
2	2850.33	24.72	0.2551	2869.20	28.80	0.1661	2903.10	29.72	0.26863	2923.95	27.81	0.5483	2953.79	16.79	0.1764
3	2851.69	24.10	0.3690	2869.74	24.35	0.1993	2903.24	31.27	0.40557	2924.51	28.08	0.8221	2954.30	17.97	0.2924
5	2851.73	26.65	0.2558	2871.50	27.43	0.1235	2903.92	30.28	0.24513	2924.59	27.99	0.5069	2954.38	17.31	0.1670
6	2851.62	21.08	0.1113	2869.65	21.95	0.0700	2903.49	30.14	0.14750	2924.62	29.23	0.3218	2954.57	18.12	0.0939
8	2847.42	46.52	0.2591	2873.65	33.66	0.0559	2904.00	36.01	0.21412	2923.28	25.15	0.1591	2952.26	15.28	0.0574
9	2851.36	21.90	0.4267	2870.96	26.45	0.1843	2902.24	29.17	0.35533	2924.56	28.08	1.0143	2955.62	16.20	0.1929
10	2845.20	20.39	0.0180	2865.84	26.59	0.0282	2904.52	36.13	0.05624	2928.18	27.23	0.0635	2954.70	17.65	0.0252

6.3 Can we estimate the H content from these data?

If we rely on the interpretation of the IR modes given above, i.e. assigning modes 1 and 4 to CH_2 clusters formed at armchair edges {AE}, and modes 2 and 5 to CH_3 clusters formed at Klein Edges {KE}, we may try to estimate the relative concentration of hydrogen in our samples from the intensity of these modes. We may write the following "chemical reaction" leading to the formation of the CH_n $(n = 2, 3)$ clusters as

$$\{\mathrm{KE}\} + 3\mathrm{H} \rightleftharpoons \mathrm{CH_3} \tag{6.1}$$

$$\{\mathrm{AE}\} + 2\mathrm{H} \rightleftharpoons \mathrm{CH_2} \tag{6.2}$$

using the law of mass action [46], for the equilibrium concentrations of the ingredients of these reactions:

$$\frac{N_{\mathrm{KE}} \cdot (N_{\mathrm{H}})^3}{N_{\mathrm{CH_3}}} = f_1(T); \tag{6.3}$$

$$\frac{N_{\mathrm{AE}} \cdot (N_{\mathrm{H}})^2}{N_{\mathrm{CH_2}}} = f_2(T); \tag{6.4}$$

where $f_1(T)$ and $f_2(T)$ are function of temperature. Dividing (6.3) by (6.4), we obtain:

$$N_{\mathrm{H}} = \left(\frac{N_{\mathrm{AE}}}{N_{\mathrm{KE}}}\right)\left(\frac{f_1(T)}{f_2(T)}\right)\left(\frac{N_{\mathrm{CH_3}}}{N_{\mathrm{CH_2}}}\right) \tag{6.5}$$

If we neglect the possible dependence of the relative concentration of armchair and Klein edges, for a fixed temperature equation (6.5) means simply that $N_{\mathrm{H}} = \text{const.}\left(\frac{N_{\mathrm{CH_3}}}{N_{\mathrm{CH_2}}}\right)$ and we can estimate $(N_{\mathrm{CH_3}}/N_{\mathrm{CH_2}})$ by the ratio of integrated intensities of the bands (2+5) and (1+4).

Taking the values of the peaks areas from Table 6.1 and normalizing to sample #2, we get:

Table 6.2: Relative concentration of hydrogen from IR-ATR spectra.

Sample	#2	#3	#5	#6	#9
Relative H concentration	1	1.033	1.119	1.126	1.629

We notice that this values considers only of hydrogen that participates in dipole-active vibrations.

7. Conclusion

In this work a set of C:H thin films grown by DCHCS on steel substrates were characterized and studied . The carbon layer thickness obtained by using SEM, after removing the substrate, ranges from 345 to 690 nm.

We performed a spectroscopic study of atomic vibration modes in hydrogenated carbon films that mimic inner coatings in tubes used in CERN accelerators. Raman spectroscopy results, supported by the analysis of the characteristic G and D modes and comparison with the literature data allow us to conclude that our samples are mostly composed of nanocrystals of graphite and/or small flakes of graphene, i.e. they are nano-graphitic rather than amorphous, with the prevalence of sp^2 bonded carbon.

A correlation was established between the background photoluminescence seen in the Raman spectra of the C:H films and the hydrogen content in the gas atmosphere during the samples' growth. The mechanisms of the correlation and the PL emission itself require further investigation.

FTIR spectroscopy studies, performed in both conventional reflection mode and ATR configuration revealed a graphite bulk plasmon signature (plasmon energy $\simeq 0.44$ eV) and contribution of five characteristic modes of stretching vibrations of C-H bonds in the range 2800 - 3000 cm^{-1}. According to the literature data, this spectral range is characteristic of sp^3-type C-H bonds. In order to reach an agreement between the mostly nano-graphitic nature of the samples (sp^2 C-C bonds) and the infrared response of sp^3-type C-H stretching vibrations, several configurations of hydrogen attached to graphite/graphene have been analysed, such as H atom sitting on top of the basal plane (1) and groups of H atoms linked to graphite/graphene armchair-type (2) and Klein-type (3) edges.

According to our lattice dynamics model, sp^3-bonded C:H clusters formed on top of the basal plane (1) and even those composed of two neighbouring structures of this kind with H atoms located at the opposite sides of the graphene sheet produce several vibration modes with very close frequencies, which are probably indistinguishable experimentally, so these clusters cannot explain the rather broad variety of features detected in the spectral range from 2850 to 2955 cm^{-1}.

Clusters (2) containing two hydrogen atoms linked to a carbon atom with two C-C bonds (sp^2-CH_2) cannot be described by the spring-mass model but the symmetry analysis of the vibrations predicts one symmetric and one asymmetric mode, both dipole-active, which are associated with the FTIR features at 2850 and 2920 cm^{-1}, observed in our samples and several other experiments performed on different forms of

hydrogenated carbon [20, 21, 22, 23, 37, 38, 47], therefore this assignment looks quite reliable.

We also assign two IR features observed in our spectra, with approximately correlated intensities through our set of samples, to 3H clusters formed at the Klein-type edges. This assignment is much less reliable because these modes were not observed in (known to us) experiments performed on nano-graphitic materials [20, 21, 22, 23, 37, 38, 47]; it is based mostly on the symmetry analysis that predicts a certain ratio between the intensities of the symmetric and asymmetric modes of the CH_3 clusters.

If this interpretation is correct, comparison of the relative intensities of the sp2-CH_2 and CH_3 (pairs of) FTIR-ATR modes allows for estimating the relative contents of hydrogen between different C:H samples.

A. Transfer matrix and Fresnel coefficients

The carbon film is a part of a multilayer structure that, in the simplest case, includes just the film and the substrate. For this kind of structures it is necessary to take into account interference effects of the electromagnetic wave at different interfaces. Interference features in the spectra can be confused with characteristic modes of the materials. The consideration of the interference effects is facilitated by using the transverse matrix method that will be described in this section.

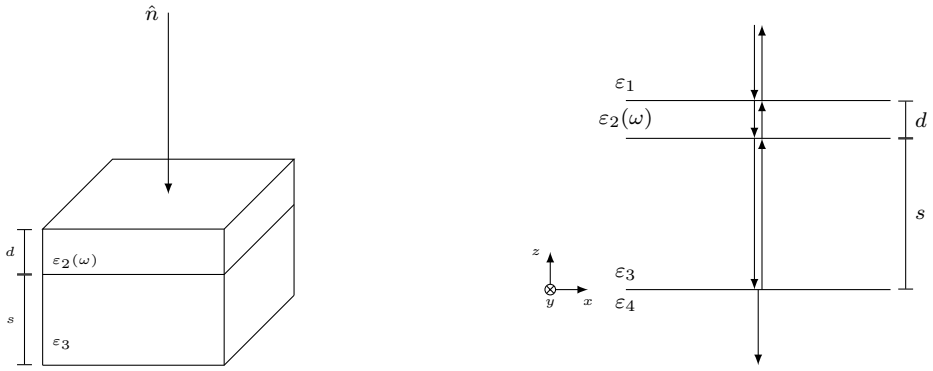

(a) **(b)**

Figure A.1: (a) Scheme of a film (thickness d) on a substrate (thickness s) width normal incidence of the light, (b) geometric representation of different layers with choice axes.

Figure A.1 shows a scheme of this kind of structures. For this normal incidence, the transversal-magnetic polarized filed can be written as:

$$H_j(\vec{r},t) = \left(e^{-ik_j z} + \hat{r}_p e^{ik_j z}\right) e^{i(k_x x - \omega t)}\hat{y} \tag{A.1}$$

where $\hat{r}_p$ is Fresnel reflection coefficient, $j = 1, 2, 3, 4$ correspond to electric and magnetic fields in different media (see Figure A.1b), where 1 and 4 correspond the air($\varepsilon_1, \varepsilon_4 = 1$), 2 is carbon film ($\varepsilon_2(\omega)$ is its dielectric function) and 3 is substrate ($\varepsilon_3 \neq 1$).

The Maxwell's equation,

$$\nabla \times \vec{H}_j(\vec{r},t) = \frac{\varepsilon_j}{c}\frac{\partial \vec{E}(\vec{r},t)}{\partial t} \tag{A.2}$$

is used to obtain the electric field in each medium:

$$\vec{E}(\vec{r},t)_j = i\frac{c}{\varepsilon_j \omega}\left(-\frac{\partial H_{y,j}}{\partial z}\hat{x} + \frac{\partial H_{y,j}}{\partial x}\hat{z}\right) \tag{A.3}$$

Then, the electric and magnetic fields in each medium can be obtained:

1. For the above surface $j = 1$ $(z > s + d)$ the fields are:

$$H_{y,1}(\vec{r},t) = \left(e^{-ik_{z,1}(z-(d+s))} + \hat{r}_p e^{ik_{z,1}(z-(d+s))}\right) e^{i(k_x x - \omega t)} \tag{A.4}$$

$$E_{x,1}(\vec{r},t) = \frac{ck_{z,}}{\omega\varepsilon_1}\left(-e^{-ik_{z,1}(z-(d+s))} + \hat{r}_p e^{ik_{z,1}(z-(d+s))}\right) e^{i(k_x x - \omega t)} \tag{A.5}$$

2. For $j = 2$ $(s < z < d)$ it gives:

$$H_{y,2}(\vec{r},t) = \left(\hat{a}e^{-ik_{z2}(z-s)} + \hat{b}e^{ik_{z2}(z-s)}\right) e^{i(k_x x - \omega t)} \tag{A.6}$$

$$E_{x,2}(\vec{r},t) = \frac{ck_{z2}}{\omega\varepsilon_2(\omega)}\left(-\hat{a}e^{-ik_{z2}(z-s)} + \hat{b}e^{ik_{z2}(z-s)}\right) e^{i(k_x x - \omega t)} \tag{A.7}$$

where $\hat{a}$ and $\hat{b}$ are unknown coefficients.

3. For $j = 3$ $(0 < z < d)$ the fields are:

$$H_{y,3}(\vec{r},t) = \left(\hat{c}e^{-ik_{z3}z} + \hat{d}e^{ik_{z3}z}\right) e^{i(k_x x - \omega t)} \tag{A.8}$$

$$E_{x,3}(\vec{r},t) = \frac{ck_{z3}}{\omega\varepsilon_3}\left(-\hat{c}e^{-ik_{z3}z} + \hat{d}e^{ik_{z3}z}\right) e^{i(k_x x - \omega t)} \tag{A.9}$$

where $\hat{c}$ and $\hat{d}$ are unknown coefficients.

4. For $j = 4$ and $z < 0$, the electric and magnetic transmitted waves are:

$$H_{y,4}(\vec{r},t) = \hat{t}_p e^{-ik_{z,4}z} e^{i(k_x x - \omega t)} \tag{A.10}$$

$$E_{x,4}(\vec{r},t) = -\frac{ck_{z,4}}{\omega\varepsilon_4}\hat{t}_p e^{-ik_{z3}z} e^{i(k_x x - \omega t)} \tag{A.11}$$

here only the transmitted wave is present, where $\hat{t}_p$ denotes the Fresnel coefficient.

The next step is to determinate the Fresnel coefficients $\hat{r}_p$ and $\hat{t}_p$. Using the boundary condition, i e. transverse component of the $\vec{E}$ and $\vec{H}$ must be continuous, it is possible to determine the Fresnel coefficients ($\hat{r}_p$ and $\hat{t}_p$) and eliminate the unknown parameters ($\hat{a}$, $\hat{b}$, $\hat{c}$ and $\hat{d}$). So, for the first interface (air/ film), corresponding to $z = (d + s)$ the boundary condition corresponds to:

$$\begin{bmatrix} H_{y,1}(\vec{r},t) \\ E_{x,1}(\vec{r},t) \end{bmatrix}_{z=(d+s)^+} = \begin{bmatrix} H_{y,2}(\vec{r},t) \\ E_{x,2}(\vec{r},t) \end{bmatrix}_{z=(d+s)^-} \tag{A.12}$$

or explicitly:

$$\begin{bmatrix} 1+\hat{r}_p \\ \frac{ck_{z,1}}{\omega\varepsilon_1}(\hat{r}_p-1) \end{bmatrix} = \begin{bmatrix} \hat{a}e^{-ik_{z2}d}+\hat{b}e^{ik_{z2}d} \\ \frac{ck_{z2}}{\omega\varepsilon_2(\omega)}\left(-\hat{a}e^{-ik_{z2}d}+\hat{b}e^{ik_{z2}d}\right) \end{bmatrix} \tag{A.13}$$

For the second interface (film/substrate), corresponding to $z = s$, the boundary condition corresponds to:

$$\begin{bmatrix} H_{y,2}(\vec{r},t) \\ E_{x,2}(\vec{r},t) \end{bmatrix}_{z=s^+} = \begin{bmatrix} H_{y,3}(\vec{r},t) \\ E_{x,3}(\vec{r},t) \end{bmatrix}_{z=s^-}. \tag{A.14}$$

In the same way as before, we obtain:

$$\begin{bmatrix} \hat{a}+\hat{b} \\ \frac{ck_{z2}}{\omega\varepsilon(\omega)}(\hat{b}-\hat{a}) \end{bmatrix} = \begin{bmatrix} \hat{c}e^{-ik_{z3}s}+\hat{d}e^{ik_{z3}s} \\ \frac{ck_{z3}}{\omega\varepsilon_3}\left(-\hat{c}e^{-ik_{z3}s}+\hat{d}e^{ik_{z3}s}\right) \end{bmatrix} \tag{A.15}$$

Finally for $z = 0$ we obtain:

$$\begin{bmatrix} \hat{c}+\hat{d} \\ \frac{ck_{z3}}{\omega\varepsilon_3}(-\hat{c}+\hat{d}) \end{bmatrix} = \begin{bmatrix} \hat{t}_p \\ -\hat{t}_p\frac{ck_{z4}}{\omega\varepsilon_4} \end{bmatrix}. \tag{A.16}$$

In this way the transfer matrices for media 2 and 3 are:

$$\begin{bmatrix} H_{y,2}(\vec{r},t) \\ E_{x,2}(\vec{r},t) \end{bmatrix}_{z=s^+} \equiv \hat{T}_a \begin{bmatrix} H_{y,2}(\vec{r},t) \\ E_{x,2}(\vec{r},t) \end{bmatrix}_{z=(d+s)^-}; \tag{A.17}$$

$$\begin{bmatrix} H_{y,3}(\vec{r},t) \\ E_{x,3}(\vec{r},t) \end{bmatrix}_{z=0^+} \equiv \hat{T}_b \begin{bmatrix} H_{y,3}(\vec{r},t) \\ E_{x,3}(\vec{r},t) \end{bmatrix}_{z=s^-}. \tag{A.18}$$

Their product gives the transfer matrix of the whole structure:

$$\begin{bmatrix} H_{y,4}(\vec{r},t) \\ E_{x,4}(\vec{r},t) \end{bmatrix}_{z=0^-} \equiv \hat{T}_T \begin{bmatrix} H_{y,1}(\vec{r},t) \\ E_{x,1}(\vec{r},t) \end{bmatrix}_{z=(d+s)^+}; \tag{A.19}$$

$$\hat{T}_T = \hat{T}_a \cdot \hat{T}_b. \tag{A.20}$$

The explicit form of layer's transfer matrix is obtained by substituting the explicit form of the fields into (A.17) or (A.18):

$$\hat{T}_a = \begin{bmatrix} \cos(k_{z2}d) & -i\frac{\omega\varepsilon_2(\omega)}{ck_{z2}}\sin(k_{z2}d) \\ -i\frac{ck_{z2}}{\omega\varepsilon_2(\omega)}\sin(k_{z2}d) & \cos(k_{z2}d) \end{bmatrix} \tag{A.21}$$

and

$$\hat{T}_b = \begin{bmatrix} \cos(k_{z3}s) & -i\frac{\omega\varepsilon_3}{ck_{z3}}\sin(k_{z3}s) \\ -i\frac{ck_{z3}}{\omega\varepsilon_3}\sin(k_{z3}s) & \cos(k_{z3}s) \end{bmatrix}. \tag{A.22}$$

Now we determinate the Fresnel coefficients from (A.19):

$$\begin{bmatrix} H_{y,1}(\vec{r},t) \\ E_{x,1}(\vec{r},t) \end{bmatrix}_{z=(d+s)^+} \equiv \hat{T}_T^{-1} \begin{bmatrix} H_{y,4}(\vec{r},t) \\ E_{x,4}(\vec{r},t) \end{bmatrix}_{z=0^-}, \tag{A.23}$$

which yields

$$\begin{bmatrix} 1+\hat{r}_p \\ \frac{ckz1}{\omega\varepsilon_1}(\hat{r}_p-1) \end{bmatrix} = \begin{bmatrix} \hat{T}_{T11} & \hat{T}_{T12} \\ \hat{T}_{T21} & \hat{T}_{T22} \end{bmatrix}^{-1} \cdot \begin{bmatrix} \hat{t}_p \\ -\frac{ck_{z4}}{\omega\varepsilon_4}\hat{t}_p \end{bmatrix}. \tag{A.24}$$

Explicitly, we have:

$$\begin{cases} 1+\hat{r}_p = \hat{T}_{T11}^{-1}\hat{t}_p - \hat{T}_{T12}^{-1}\frac{ck_{z4}}{\omega\varepsilon_4}\hat{t}_p \\ \frac{ck_{z1}}{\omega\varepsilon_1}(\hat{r}_p-1) = \hat{T}_{T21}^{-1}\hat{t}_p - \hat{T}_{T22}^{-1}\frac{ck_{z4}}{\omega\varepsilon_4}\hat{t}_p \end{cases} \tag{A.25}$$

and solving the equation system in terms Fresnel coefficients we obtain:

$$\hat{r}_p = \hat{t}_p\left(\hat{T}_{T11}^{-1} - \hat{T}_{T12}^{-1}\frac{ck_{z4}}{\omega\varepsilon_4}\right) - 1 \tag{A.26}$$

$$\hat{t}_p = \frac{2}{\hat{T}_{t11}^{-1} - \hat{T}_{T12}^{-1}\frac{ck_{z4}}{\omega\varepsilon_4} - \hat{T}_{T21}^{-1}\frac{\omega\varepsilon_1}{ckz1} + \hat{T}_{T22}^{-1}\frac{k_{z4}\varepsilon_1}{\varepsilon_4 k_{z1}}} \tag{A.27}$$

(recall that the total transfer matrix is product between two transfer matrix each layer). For a system with more layers number is treated in the same way, only needs to construct the transfer matrix like equation A.21 and A.22, and add a the total transfer matrix as product:

$$\hat{T}_T = \prod_{j=1}^{n} \hat{T}_j \tag{A.28}$$

where n is the number of different layers.

B. Processing of experimental data

B.1 Raman spectra

As mentioned in Section 6.1, PL background in the Raman spectra can be approximated by a linear function of frequency. The following figure demonstrates this procedure.

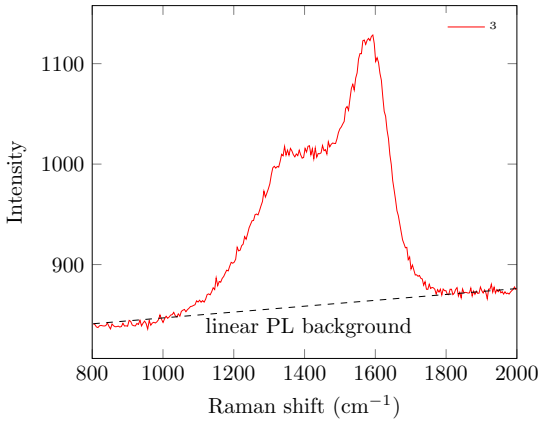

After removing the background, we can see in the next set of figures the spectra of all samples fitted with three Lorenzians in the range of 800-2000 cm^{-1}.They have been used to determine positions D and G modes, and their intensities as well as FWHM. This procedure was applied after the background photoluminescence has beer removed.

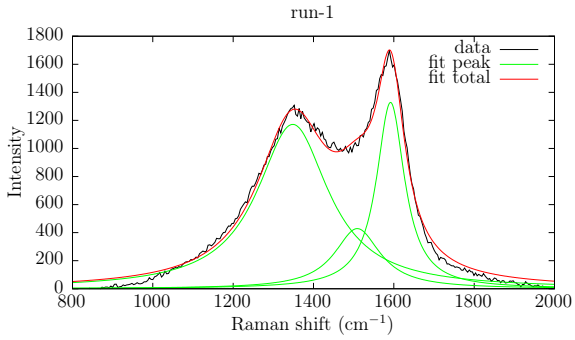

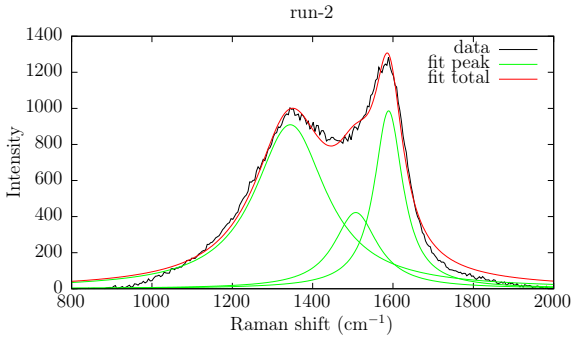

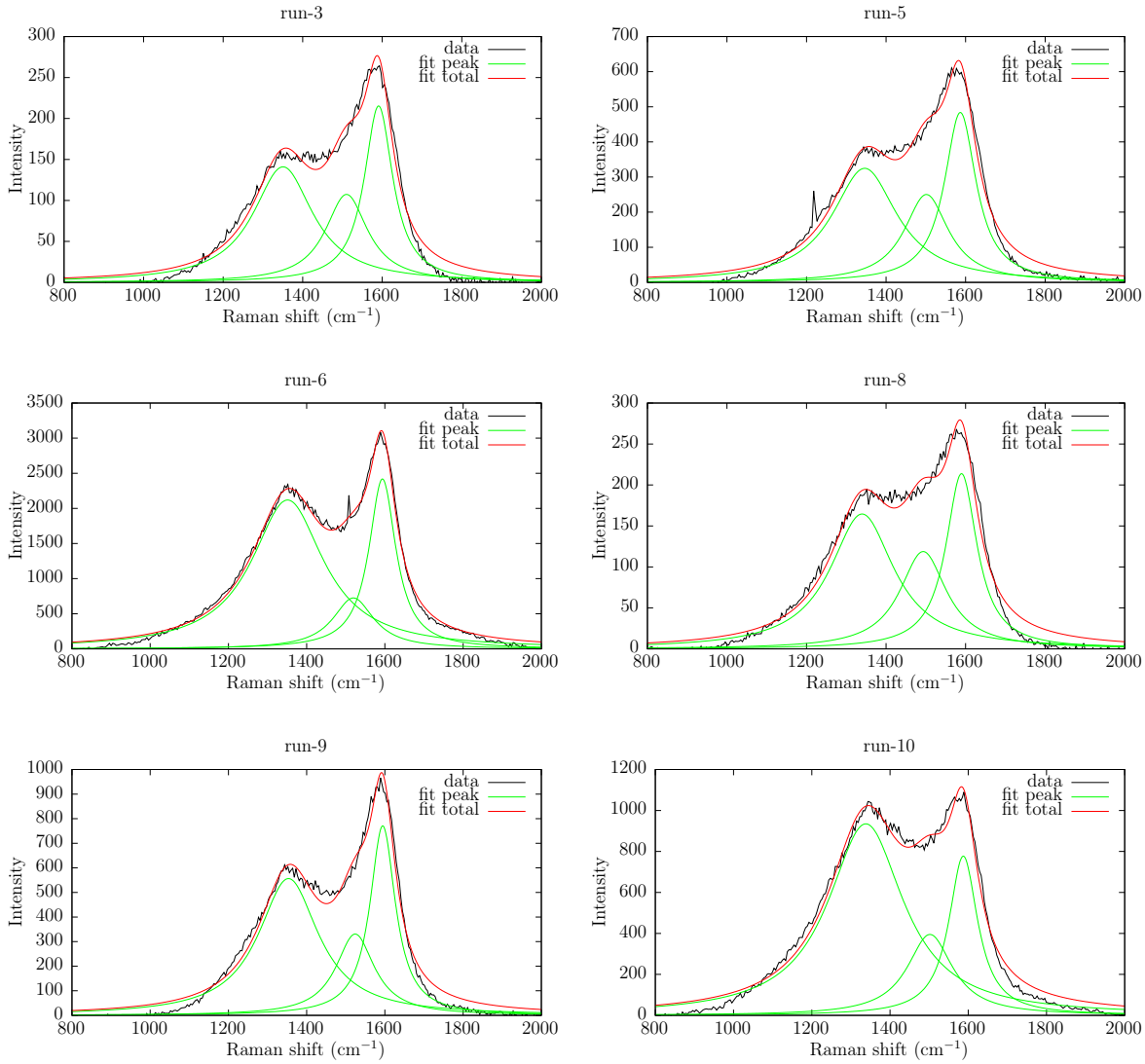

B.2 FTIR-ATR spectra

Based on the FTIR-ATR spectra, we calculated $[1 - R_{ATR}(\omega)]$. The results are shown in the next set of figures in the C-H range.

We performed the fitting using five Lorentzians functions to determinate frequencies od the C-H modes as well as their intensities for samples, with reasonable intensity in this range.

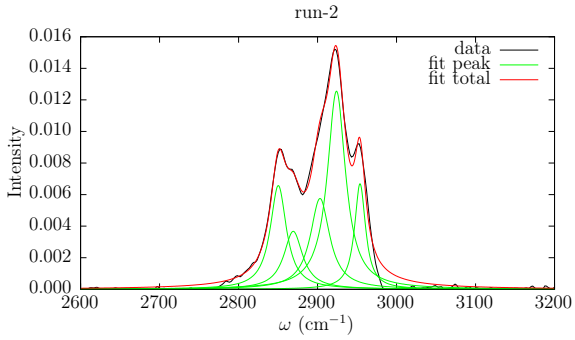
run-2
data
fit peak
fit total
Intensity
ω (cm⁻¹)

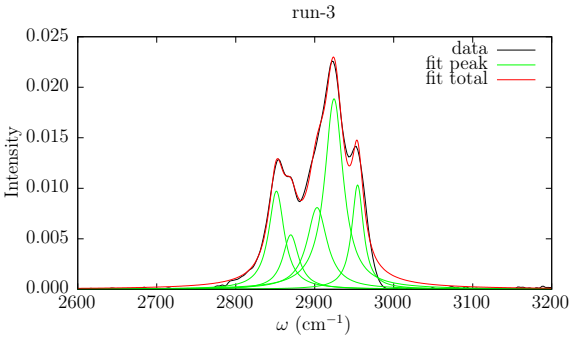
run-3
data
fit peak
fit total
Intensity
ω (cm⁻¹)

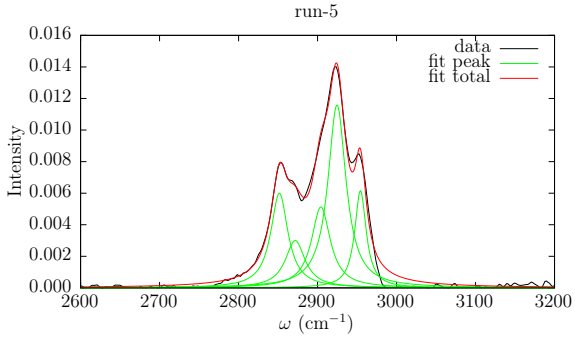
run-5
data
fit peak
fit total
Intensity
ω (cm⁻¹)

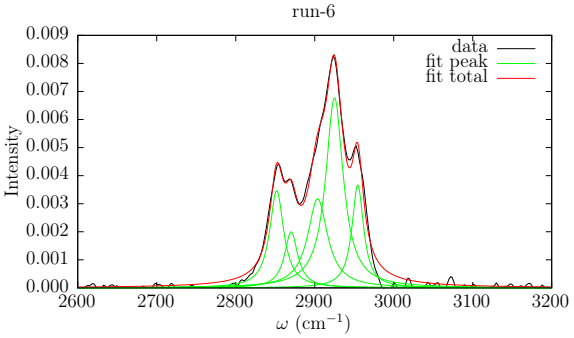
run-6
data
fit peak
fit total
Intensity
ω (cm⁻¹)

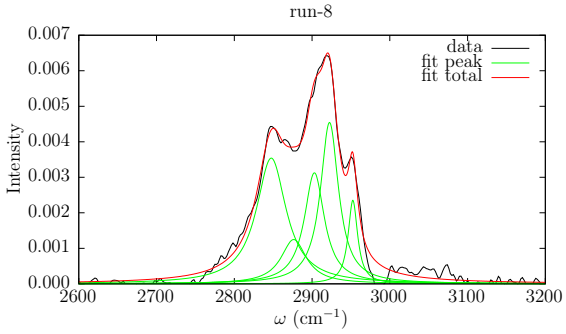
run-8
data
fit peak
fit total
Intensity
ω (cm⁻¹)

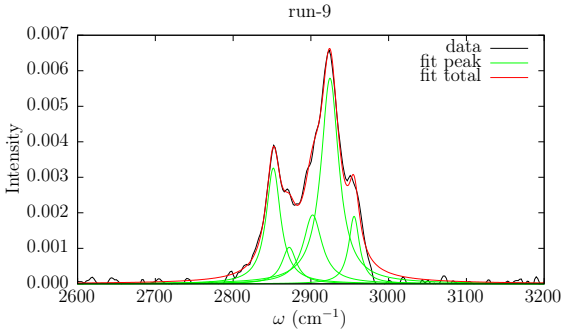
run-9
data
fit peak
fit total
Intensity
ω (cm⁻¹)

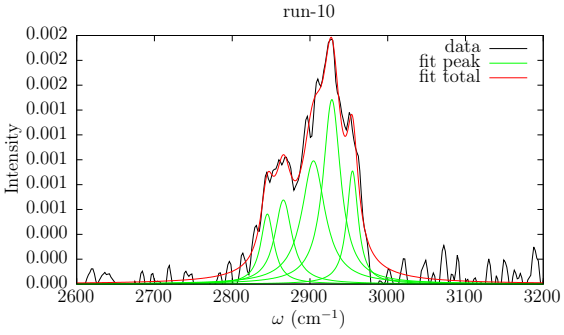
run-10
data
fit peak
fit total
Intensity
ω (cm⁻¹)

Bibliography

[1] J Robertson. Diamond-like amorphous carbon. *Materials Science and Engineering: R: Reports*, 37(4-6):129–281, 2002.

[2] Fridman. Surface and Structural Analysis of Carbon Coatings Produced by Plasma Jet CVD. *Materials Science*, 13(4):1–4, 2007.

[3] G. Lazar, K. Zellama, I. Vascan, M. Stamate, I. Lazar, and I. Rusu. Infrared absorption properties of amorphous carbon films. *Journal of Optoelectronics and Advanced Materials*, 7(2):647–652, 2005.

[4] Sarah Aull, Tobias Junginger, Jens Knobloch, and Holger Neupert. Secondary electron yield of SRF materials. page TUPB050. 5 p, 2015.

[5] E. Fitzer and Lalit M. Manocha. *Friction and Wear Properties of Carbon/Carbon Composites*, pages 263–280. Springer Berlin Heidelberg, Berlin, Heidelberg, 1998.

[6] M G Beghi, A C Ferrari, K B K Teo, J Robertson, C E Bottani, A Libassi, and B K Tanner. Bonding and mechanical properties of ultrathin diamond-like carbon films. *Applied Physics Letters*, 81(20):3804–3806, nov 2002.

[7] Paul K Chu and Liuhe Li. Characterization of amorphous and nanocrystalline carbon films. *Materials Chemistry and Physics*, 96(2-3):253–277, apr 2006.

[8] A K Geim and K S Novoselov. The rise of graphene. *Nature Materials*, 6(3):183–191, mar 2007.

[9] A C Ferrari and J Robertson. Raman spectroscopy of amorphous, nanostructured, diamond-like carbon, and nanodiamond. *Philosophical Transactions of the Royal Society A: Mathematical, Physical and Engineering Sciences*, 362(1824):2477–2512, nov 2004.

[10] J Robertson and E P O'Reilly. Electronic and atomic structure of amorphous carbon. *Physical Review B*, 35(6):2946–2957, feb 1987.

[11] T. Paulmier, J.M. Bell, and P.M. Fredericks. Deposition of nano-crystalline graphite films by cathodic plasma electrolysis. *Thin Solid Films*, 515(5):2926–2934, jan 2007.

[12] Klaus Bewilogua and Dieter Hofmann. History of diamond-like carbon films – From first experiments to worldwide applications. *Surface and Coatings Technology*, 242:214–225, mar 2014.

[13] S. A. Solin and A. K. Ramdas. Raman spectrum of diamond. *Physical Review B*, 1(4):1687–1698, 1970.

[14] Gert Irmer and Annett Dorner-Reisel. Micro-Raman studies on DLC coatings. *Advanced Engineering Materials*, 7(8):694–705, 2005.

[15] F Tuinstra and J L Koenig. Raman Spectrum of Graphite. *The Journal of Chemical Physics*, 53(3):1126–1130, aug 1970.

[16] J Schwan, S Ulrich, V Batori, H Ehrhardt, and S R P Silva. Raman spectroscopy on amorphous carbon films. *Journal of Applied Physics*, 80(1):440–447, jul 1996.

[17] J G Buijnsters, R Gago, I Jiménez, M Camero, F Agulló-Rueda, and C Gómez-Aleixandre. Hydrogen quantification in hydrogenated amorphous carbon films by infrared, Raman, and x-ray absorption near edge spectroscopies. *Journal of Applied Physics*, 105(9):93510, may 2009.

[18] K Nakamoto. *Infrared Spectra of Inorganic and Coordination Compounds*. Wiley, 1963.

[19] Manuel Melle-Franco. *Private communication*, 2018.

[20] Liutauras Marcinauskas, Alfonsas Grigonis, Vitas Valincius, and Pranas Valatkevicius. Surface and structural analysis of carbon coatings produced by plasma jet cvd. *Mater. Sci*, 13(269):e272, 2007.

[21] Adarsh Kaniyoor, R Imran Jafri, T Arockiadoss, and S Ramaprabhu. Nanostructured pt decorated graphene and multi walled carbon nanotube based room temperature hydrogen gas sensor. *Nanoscale*, 1(3):382–386, 2009.

[22] Alex Yong Sheng Eng, Hwee Ling Poh, Filip Sanek, Miroslav Marysko, Stanislava Matejkova, Zdenek Sofer, and Martin Pumera. Searching for magnetism in hydrogenated graphene: using highly hydrogenated graphene prepared via birch reduction of graphite oxides. *Acs Nano*, 7(7):5930–5939, 2013.

[23] Ricarda A Schäfer, Jan M Englert, Peter Wehrfritz, Walter Bauer, Frank Hauke, Thomas Seyller, and Andreas Hirsch. On the way to graphane-pronounced fluorescence of polyhydrogenated graphene. *Angewandte Chemie International Edition*, 52(2):754–757, 2013.

[24] M. H. Brodsky, Manuel Cardona, and J. J. Cuomo. Infrared and Raman spectra of the silicon-hydrogen bonds in amorphous silicon prepared by glow discharge and sputtering. *Physical Review B*, 16(8):3556–3571, 1977.

[25] Vasilica Tucureanu, Alina Matei, and Andrei Marius Avram. FTIR Spectroscopy for Carbon Family Study. *Critical Reviews in Analytical Chemistry*, 46(6):502–520, 2016.

[26] G Bauer and W Richter. *Optical Characterization of Epitaxial Semiconductor Layers*. Springer Berlin Heidelberg, Berlin, Heidelberg, 1996.

[27] Hans Kuzmany. *Solid-State Spectroscopy: An Introduction*. Springer Berlin Heidelberg, 1998.

[28] F.M. Mirabella. *Internal Reflection Spectroscopy: Theory and Applications*. Practical Spectroscopy. Taylor & Francis, 1992.

[29] T. Dumelow, T.J. Parker, S.R.P. Smith, and D.R. Tilley. Far-infrared spectroscopy of phonons and plasmons in semiconductor superlattices. *Surface Science Reports*, 17(3):151 – 212, 1993.

[30] L Novotny and B Hecht. *Principles of Nano-Optics*. Cambridge University Press, 2012.

[31] J R Tesmer and M A Nastasi. *Handbook of Modern Ion Beam Materials Analysis*. Mrs Symposium Proceedings Series. Materials Research Society, 1995.

[32] Filipe André Peixoto Oliveira. *Raman Spectroscopy Studies of Sn Ge and x 1-x ZnO:Mn Semiconductor Solid Solutions*. PhD thesis, 2018.

[33] Kenichiro Mizohata. *Progress in Elastic Recoil Detection Analysis*. 2012.

[34] A C Ferrari and J Robertson. Interpretation of Raman spectra of disordered and amorphous carbon. *Phys. Rev. B*, 61(20):95–107, 2000.

[35] Björn Karlsson and Carl G. Ribbing. Optical constants and spectral selectivity of stainless steel and its oxides. *Journal of Applied Physics*, 53(9):6340–6346, 1982.

[36] Q.X. Pei, Y.W. Zhang, and V.B. Shenoy. A molecular dynamics study of the mechanical properties of hydrogen functionalized graphene. *Carbon*, 48(3):898 – 904, 2010.

[37] Philipp Wagner, Viktoria V. Ivanovskaya, Manuel Melle-Franco, Bernard Humbert, Jean-Joseph Adjizian, Patrick R. Briddon, and Christopher P. Ewels. Stable hydrogenated graphene edge types: Normal and reconstructed klein edges. *Phys. Rev. B*, 88:094106, Sep 2013.

[38] M Vandescuren, P Hermet, V Meunier, L Henrard, and Ph Lambin. Theoretical study of the vibrational edge modes in graphene nanoribbons. *Physical Review B*, 78(19):195401, 2008.

[39] Herbert R. Philipp. Infrared optical properties of graphite. *Physical Review B*, 16(6):2896–2900, 1977.

[40] E. A. Taft and H. R. Philipp. Optical properties of graphite. *Phys. Rev.*, 138:A197–A202, Apr 1965.

[41] M Badioli, A Woessner, K J Tielrooij, S Nanot, G Navickaite, T Stauber, F J García De Abajo, and F H L Koppens. Supplementary online material for Phonon-mediated mid-infrared photoresponse of graphene Dependence of the photocurrent on the excitation power Perpendicular polarization. *Nano Lett.*, pages 1–9, 2014.

[42] M. A. Ordal, Robert J. Bell, R. W. Alexander, L. L. Long, and M. R. Querry. Optical properties of fourteen metals in the infrared and far infrared: Al, Co, Cu, Au, Fe, Pb, Mo, Ni, Pd, Pt, Ag, Ti, V, and W. *Applied Optics*, 24(24):4493, 1985.

[43] C. Casiraghi, F. Piazza, A.C. Ferrari, D. Grambole, and J. Robertson. Bonding in hydrogenated diamond-like carbon by raman spectroscopy. *Diamond and Related Materials*, 14(3):1098 – 1102, 2005. Proceedings of Diamond 2004, the 15th European Conference on Diamond, Diamond-Like Materials, Carbon Nanotubes, Nitrides and Silicon Carbide.

[44] C. Casiraghi. Effect of hydrogen on the UV Raman intensities of diamond-like carbon. *Diamond and Related Materials*, 20(2):120–122, 2011.

[45] M. N. Ess, D. Ferry, E. D. Kireeva, R. Niessner, F. X. Ouf, and N. P. Ivleva. In situ Raman microspectroscopic analysis of soot samples with different organic carbon content: Structural changes during heating. *Carbon*, 105:572–585, 2016.

[46] L. D. Landau E. M. Lifshitz. *Statistical Physics, Part 1*, volume 5 of *Course of theoretical physics*. Pergamon Press, 1969.

[47] Eunice Cunha, Maria Fernanda Proença, Florinda Costa, António J Fernandes, Marta AC Ferro, Paulo E Lopes, Mariam González-Debs, Manuel Melle-Franco, Francis Leonard Deepak, and Maria C Paiva. Self-assembled functionalized graphene nanoribbons from carbon nanotubes. *ChemistryOpen*, 4(2):115–119, 2015.